



universität
wien

MASTERARBEIT / MASTER'S THESIS

Titel der Masterarbeit / Title of the Master's Thesis

Automated electron-beam manipulation of graphene impurities

verfasst von / submitted by

Somar Dibeh

angestrebter akademischer Grad / in partial fulfilment of the requirements for the degree of
Master of Science (MSc)

Wien, 2023 / Vienna, 2023

Studienkennzahl lt. Studienblatt /
degree programme code as it appears on
the student record sheet:

UA 066 876

Studienrichtung lt. Studienblatt /
degree programme as it appears on
the student record sheet:

Masterstudium Physik

Betreut von / Supervisor:

Assoz. Prof. Dr. Toma Susi

Abstract

Graphene, the two-dimensional material, has gained significant attention due to its exceptional properties and the huge potential for being integrated in various future applications. In recent years, aberration-corrected scanning transmission electron microscopy (STEM) has been employed not only for atomic resolution imaging but also for defect engineering in graphene and other low-dimensional materials.

In this thesis, our focus lies on investigating point defects in graphene. We begin by introducing vacancies into the graphene lattice, followed by the incorporation of Al single-atom impurities into these created defects. The characterization and analysis of these defects will be carried out using scanning transmission electron microscopy. Moreover, we utilize the focused electron probe of STEM to modify the structure of the graphene sample by manipulating and precisely repositioning embedded impurities.

This work addresses the physical and instrumental limitations that can hinder successful automated single-atom manipulation in graphene, as well as generating insights on the scalability and controllability of the automated manipulation process. The thesis includes successful automated manipulation of both Si and Al single-atom impurities, along with the observation of other dynamics occurring under the electron beam during the manipulation process.

Kurzfassung

Graphen ist ein zweidimensionales Material, welches, aufgrund seiner außergewöhnlichen Eigenschaften und seines großen Potenzials für die Integration in verschiedene künftige Anwendungen, große Aufmerksamkeit erregt hat. In den letzten Jahren wurde die aberrationskorrigierte Rastertransmissionselektronenmikroskopie (STEM) nicht nur für die Bildgebung mit atomarer Auflösung eingesetzt, sondern auch für die gezielte Erzeugung und Manipulation von Defekten in Graphen und anderen niedrigdimensionalen Materialien eingesetzt.

In dieser Arbeit liegt unser Schwerpunkt auf der Untersuchung von Punktdefekten in Graphen. Leerstellen werden in das Graphengitter eingebracht, welche anschließend mit einzelnen Aluminiumatomen gefüllt werden. Damit erzeugt man kovalent gebundene Al-Heteroatome im Graphengitter. Die Charakterisierung und Analyse dieser Defekte wird mit Hilfe der Rastertransmissionselektronenmikroskopie durchgeführt. Der fokussierte Elektronenstrahl wird außerdem verwendet, um die Struktur der Probe zu verändern, indem wir die eingebetteten Heteroatome manipuliert und präzise neu positioniert werden.

Diese Arbeit befasst sich mit den physikalischen und instrumentellen Beschränkungen, die eine erfolgreiche automatisierte Manipulation einzelner Atome in Graphen behindern können und liefert Erkenntnisse über die Skalierbarkeit und Kontrollierbarkeit des automatisierten Manipulationsprozesses. Die Arbeit umfasst die erfolgreiche automatisierte Manipulation von einzelnen kovalent gebundenen Si- und Al-Atomen durch den Elektronenstrahl sowie die Beobachtung anderer dynamischer Prozesse während des Manipulationsprozesses.

Acknowledgements

To my little son, Khaled, for his patience during my master's degree, and I promise to make up for the missed playing time with him in the future. To his beautiful mother, my beloved Soha Mustafa, for her unconditional love and support. To my family, especially my parents in Syria, for their love and support. To Laurie Davidson, my dear friend, who has become an integral part of our small family. I am thankful for your support and for the assistance in improving my English skills.

I would like to express my sincere thanks to my supervisor, Assoz. Prof. Dr. Toma Susi, for his continuous support throughout the entire duration of this thesis. His constructive feedback was instrumental in its completion. My gratitude also extends to Univ.-Prof. Dr. Jani Kotakoski, the leader of our research group.

My heartfelt gratitude goes to Dr. Andreas Postl, who joined me during the first two months of my experimental work, for his kindness and support. I would also like to express my thanks to Dr. Kimmo Mustonen for his support and assistance with the deposition process. Additionally, I am grateful to my colleague, Wael Joudi, for his help with plasma irradiation. To Manuel Längle for providing the ion beam current measurements data and helping with the German version of the abstract of this thesis. My immense thanks go to the incredibly nice and helpful Dr. Clemens Mangler for his support throughout my experimental work, addressing all the technical and software issues that I encountered.

I would like to express my gratitude to all the colleagues who supported me and were part of this journey during my master's study. I appreciate the nice time I spent with them and would like to thank those with whom I shared an office, hoping not to forget anyone: Thi Thuy An Bui, Alexandru Chirita, Diana Propst, Carsten Speckmann, Manpreet Kaur, Daniel Imrich, David Lamprecht, Fabian Kraft, Clara Kofler, Helena Kempf, Kathrin Linke, Shrirang Chokappa, Leonel Cabrera, Jana Dzibelova, Barbara Mayer, Harriet Åhlgren, Arixin Bo, and Jacob Madsen.

Contents

1	Introduction	1
1.1	Motivation	1
1.2	Graphene	2
1.3	Point defects in graphene	3
1.3.1	Vacancies	4
1.3.2	Stone-Wales defect	6
1.3.3	Substitutional impurities and carbon adatoms	7
1.4	Diffusion of defects	9
1.5	Irradiation effect of energetic electrons in graphene	10
1.5.1	Knock-on damage of carbon atoms	10
1.5.2	Knock-on displacement of impurity atoms	13
1.6	Impurity atom manipulation in graphene	13
1.6.1	Direct exchange	14
1.6.2	Stone-Wales rotation	15
1.6.3	Replacement of dopants by C adatoms	15
1.6.4	Ejection of one of the neighboring C atoms	15
2	Methods	16
2.1	Scanning transmission electron microscopy	16
2.1.1	STEM imaging system	17
2.1.2	Annular dark field detection	17
2.1.3	Nion UltraSTEM 100	18
2.2	Electron energy-loss spectroscopy	19
2.3	Low-energy ions for defect engineering	21
2.4	Sample preparation	22
2.4.1	TEM grids and graphene films	22
2.4.2	Graphene transfer and removing PMMA	22
2.5	In situ sample processing	23
2.5.1	Microwave Ar ⁺ plasma source for vacancy formation	24
2.5.2	Thermal evaporation of Al impurities onto graphene	26
2.6	Automated single-atom manipulation	27
2.6.1	Nion Swift Atom Manipulator plugin	28
2.6.2	Experimental procedure and data acquisition	29
3	Results and discussion	32
3.1	Laser cleaning effect	32
3.2	Vacancies and nanopores after plasma irradiation	33

3.3	Incorporation of Al into the graphene lattice	39
3.3.1	Distinguishing between Al and Si atoms	39
3.4	Automated single-atom manipulation	40
3.4.1	Efficiency of manipulation in the presence of competing processes	41
3.4.2	Six successful controlled jumps of a Si dopant	42
3.4.3	Replacement of Si by C	45
3.4.4	Ejection of C neighbor to Al	45
3.4.5	Successful automated manipulation of Al dopant	46
3.4.6	Ejection of Al	46
3.5	Challenges and limitations	50
4	Conclusion	51
	Bibliography	52

1 Introduction

1.1 Motivation

Since its discovery in 2004 by Novoselov and Geim [1], graphene has emerged as a central point of research in the field of material science and nanostructured materials. Graphene, a remarkable two-dimensional (2D) carbon-based material, exhibits exceptional properties [2], including outstanding thermal and electrical conductivity [3], as well as remarkable mechanical strength as the thinnest and strongest material ever made [4]. However, the ability to tailor these properties according to specific needs is crucial for its integration into practical applications. Heteroatom doping of graphene and the subsequent control and manipulation of the incorporated dopants within the lattice offers the potential to achieve this objective [5].

The manipulation of individual atoms using a scanning tunneling microscope (STM) was first demonstrated in the late 1980s [6]. This was done by utilizing the STM tip to precisely move molecules and even create patterns and draw letters. However, this remarkable achievement comes with the drawback of the requirement for cryogenic conditions to ensure stability and control during the manipulation process. Additionally, only weakly bound surface atom can be manipulated and the STM tip has to be mechanically moved, adding complexity to the procedure [7].

After significant advancements in scanning transmission electron microscopy (STEM), particularly with the introduction of aberration correction, STEM has emerged not only as a powerful imaging technique with sub-Ångstrom resolution, but also as an engineering tool for material modifications at the atomic scale [8]. In 2D materials like graphene, the focused STEM electron probe provides the capability to precisely direct electrons at specific atoms, while its high energy enables the breaking and reformation of covalent bonds of the irradiated material [7]. Notably, these manipulations can be carried out at room temperature, giving STEM advantage over STM when it comes to single-atom manipulation.

In 2014, an intriguing phenomenon was discovered during STEM imaging, where a single Si heteroatom embedded in graphene was observed to jump through the lattice under 60 keV electron irradiation. This observation triggered further research led by Prof. Toma Susi and cooperators to investigate this interesting behavior and explore the ability of manipulating single-atom impurities in graphene using the energetic electrons. While 34 lattice jumps of a Si dopant in graphene by manually parking the electron probe on

1 Introduction

the target Si atom was recorded, practical applications demand automated manipulation techniques, particularly for large-scale patterning. To address this issue, team members Dr. Andreas Postl and Dr. Jacob Madsen developed a software that enables automated single-atom manipulation using STEM.

While the majority of studies on single-atom manipulation have focused on Si atoms, there have been only few reports on other impurities, including the manipulation of P [9], and the dynamic of Al single atoms [10]. The main goal of this work was to investigate automated single-atom manipulation of both Si and Al impurities and, if possible, to draw a pattern composed of at least three impurity atoms. For this purpose, a graphene sample with Al dopants was prepared via a two-step implantation process, while the sample with Si impurities was available from prior work.

In this section the reader will be familiarized with the fundamental theoretical concepts related to point defects in graphene, as well as the different processes of irradiation effects that occur under the electron beam in a STEM that are relevant to single-atom manipulation.

1.2 Graphene

Carbon is the sixth element in the periodic table with an electronic configuration of $1s^2 2s^2 2p^2$ in its ground state. Carbon can exhibit different forms of hybridization [11]. Graphite is formed when one $2s$ orbital combines with two $2p$ orbitals, leading to three bonds with sp^2 hybridisation. Graphene is a 2D material formed simply from one layer of graphite. The three sp^2 hybrid orbitals of carbon in graphene bond with other sp^2 orbitals of the nearest carbon atoms. These σ bonds are strong covalent bonds and result in the planar hexagonal crystal structure of graphene, with an angle of 120° between the sp^2 orbitals [12]. Graphene has therefore a honeycomb crystal lattice with lattice vectors given by

$$\vec{\mathbf{a}}_1 = \frac{a}{2}(3, \sqrt{3}) \quad \vec{\mathbf{a}}_2 = \frac{a}{2}(3, -\sqrt{3}), \quad (1.1)$$

where $a \approx 1.42 \text{ \AA}$ is the distance between two nearest carbon neighbors and $|\vec{\mathbf{a}}_1| \approx 2.46 \text{ \AA}$ is the lattice constant in graphene [13]. The unit cell comprises two atoms, A and B, belonging to different sublattices, as illustrated in Figure 1.1.a with blue and red colors. The reciprocal lattice vectors can be obtained using the relation between them and the vectors in real space

$$\vec{\mathbf{b}}_i \cdot \vec{\mathbf{a}}_j = 2\pi\delta_{ij}, \quad (1.2)$$

which gives

$$\vec{\mathbf{b}}_1 = \frac{2\pi}{3a}(1, \sqrt{3}) \quad \vec{\mathbf{b}}_2 = \frac{2\pi}{3a}(1, -\sqrt{3}). \quad (1.3)$$

The remaining valence electron in the $2p_z$ orbitals forms the perpendicular π (bonding) and the π^* (anti-bonding) orbitals, which represent the valence and conduction bands in

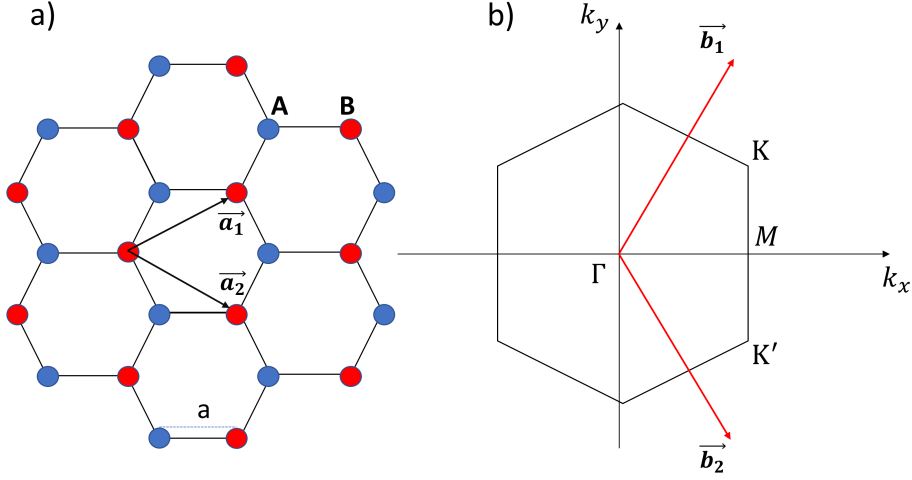


Figure 1.1: (a) Honeycomb lattice of graphene illustrating the lattice vectors \vec{a}_1 , \vec{a}_2 and the two sublattices A and B, represented by blue and red colors, respectively. (b) The first Brillouin zone in the reciprocal lattice of graphene, highlighting its high-symmetry points.

graphene, respectively. These perpendicular π orbitals are responsible for the van der Waals weak interactions between graphite layers. The reciprocal lattice of graphene is hexagonal, and the first Brillouin zone, constructed from the Wigner-Seitz cell of the reciprocal lattice, is depicted in Figure 1.1.b. The totally filled valence band π and empty conduction band π^* of pristine graphene cross at the six high-symmetry points K and K' , where the Fermi level lies. For this reason, graphene is described as a gapless semiconductor [14].

Graphene exhibits a linear dispersion at these K points in the electronic band structure. However, the unique electronic properties of graphene do not solely originate from being gapless or having a linear dispersion at the K points, but also from the distinctive chirality of its electronic state (dispersion relations are not the same for K , K' points) and the pronounced electron-hole symmetry [13, 14]. In fact, the absence of the band gap in pristine graphene is generally not desired for most electronic applications [15]. On the other hand, the deliberate introduction of defects in graphene and engineering them in a controlled manner can be of a great advantage for various applications [16].

1.3 Point defects in graphene

Imperfections in a crystalline solid can be defined as deviations from the regular arrangement of atoms, in which the local symmetry in the vicinity of the defect is broken. The presence of imperfections in real crystals is inevitable and can significantly alter the properties of materials, introducing a serious challenge for many applications [17].

1 Introduction

However, having imperfections can also be advantageous and a necessity for tailoring material properties for certain applications [15]. The types of defects that can be present in graphene are limited due to its low dimensionality, thus confined to just line or point defects [16]. Regarding atom manipulation using STEM, line defects such as dislocations or grain boundaries are not relevant since we deliberately avoid them by selecting the appropriate field of view (FOV) during the experiment. Our main focus will be point defects, which will be discussed in the next section.

1.3.1 Vacancies

The presence of vacancies and multi-vacancy complexes in graphene not only can induce magnetism [18, 19], but it can also drastically alter its mechanical, electrical, and chemical properties [20].

The simplest point defect is the single vacancy (SV), which can be formed by removing one carbon atom from its lattice site through a non-equilibrium process. This process is most common during irradiation, where collisions with energetic particles lead to the creation of SVs [20]. When a single vacancy is formed, three carbon atoms are left with a dangling bond each at the vacant site. Subsequently, two of these three carbon atoms weakly bond together, resulting in a local configuration that undergoes a spontaneous Jahn-Teller distortion. This leads to the formation of a pentagon and one remaining dangling bond at the vacant site, which is referred to as the (5-9) defect [20, 21]. The formation energy of a SV is about 7.5 eV, and the switching between the three degenerate asymmetric configurations can in the absence of strain be readily achieved by overcoming an energy barrier of 0.1 eV [16, 21, 22].

When two SVs unite or two neighbouring carbon atoms are removed from the lattice, a divacancy (DV) can be formed. This results in the formation of a pentagon-octagon-pentagon structure (5-8-5), which replaces the four hexagons in the corresponding location of the perfect lattice, as depicted in the Figure 1.2.b. The formation energy of the (5-8-5) defect is almost the same as a SV, 8 eV, indicating a lower energy per missing atom compared to a SV. This makes the formation of DVs energetically more favourable. By rotating one of the octagon bonds in the (5-8-5) defect, it can transform into a three pentagon and three heptagon (555-777) defect, as depicted in Figure 1.2.c. The (555-777) defect has a lower formation energy of 7 eV, making it even more stable than the (5-8-5) defect.

When more than two neighboring atoms are missing, this leads to a larger vacancy complex. Vacancy configurations with no dangling bonds, which is the case with for an even number of missing carbon atoms, are energetically more favored and stable [16]. Figure 1.2 shows images obtained from our experiment of a (5-9) SV defect, as well as both a (5-8-5) and (555-777) DVs, along with their corresponding calculated atomic structures [16].

All the aforementioned types of vacancies are intrinsic since the removed atoms are carbon and no foreign heteroatoms are present [23]. For the purpose of atom manipulation, the introduction of SVs and DVs in the sample was essential for incorporating single heteroatoms into them. This was achieved by using plasma irradiation, which will be described in detail in the experimental method section.

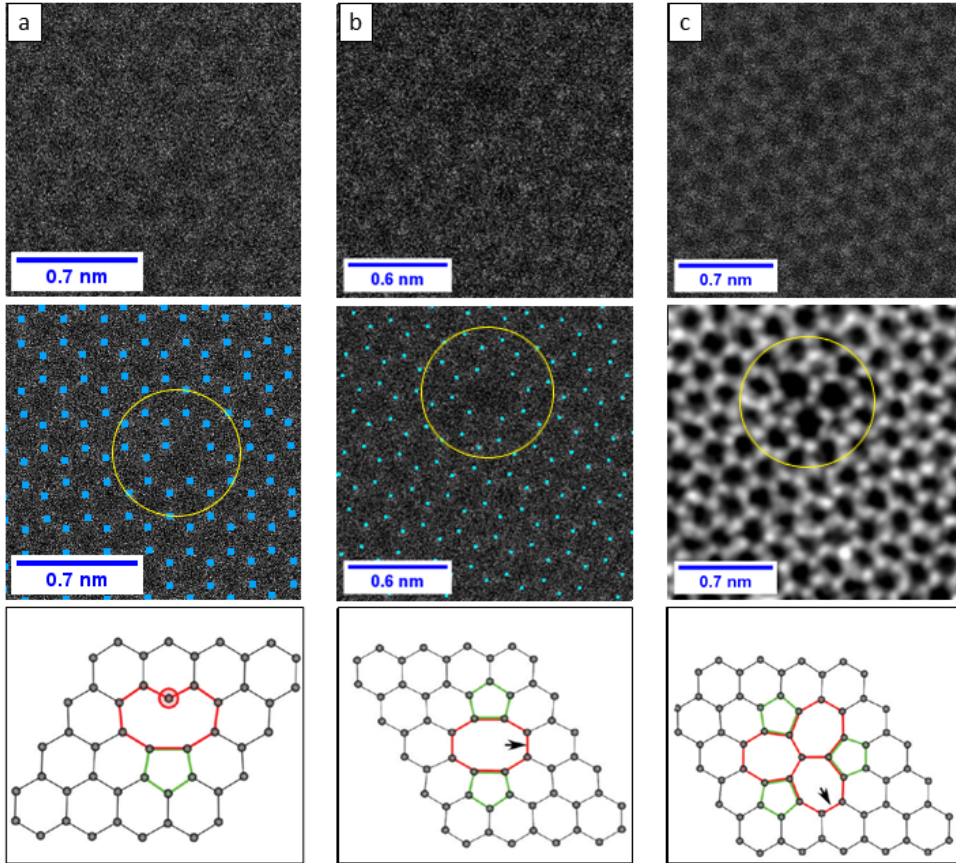


Figure 1.2: Different vacancy defect types in graphene. (a) MAADF image (top) acquired during our experiment of a SV defect (5-9) accompanied with an image (middle) of the same area with an overlay defining the atomic locations in the lattice. In the bottom, the corresponding simulated reconstructed structure of the same defect is shown. (b) A MAADF image (top) of a DV defect (5-8-5) with its corresponding structure recognition image (middle). A simulation of the same (5-8-5) defect: the arrow pointing to the bond indicates that by rotating this bond the defect transform to the type (555-777). (c) A raw image (top) of the (555-777) divacancy defect with its corresponding Gaussian filtered image (middle). Simulated structure (bottom) of the (555-777) defect. (Simulations adapted with permission from Ref. [16]. Copyright 2011 American Chemical Society.)

1.3.2 Stone-Wales defect

The Stone-Wales (SW) bond rotation in graphene transforms four proximal hexagons into a pentagon-heptagon double pair denoted as SW(55-77) shown in Figure 1.3. This topological defect favoured structure strain as in carbon nanotubes [24] and play an essential rule in the plasticity of carbon nanotubes and it affects their electronic properties through changing their chirality [25].

The formation energy of the SW defect ranges between 5 to 6.3 eV [25] and has to overcome an energy barrier of 10 eV when formed via a 90° bond rotation of two carbon atoms around their joint center [16]. Due to the high formation energy of SW defects, they have very low equilibrium concentration at room temperature. The defects can be generated when the graphene sheet is irradiated by energetic particles as in STEM and the high reverse transformation energy of ca. 5 eV ensures their thermal stability at room temperature [16, 24].

SW defects are intrinsic like vacancy defects [23], but unlike the formation of vacancies, the number of atoms in SW defects is conserved. In our experiments, 60 keV energetic electrons are used for imaging and for atom manipulations, thus the formation of SW defects is readily achieved under the electron beam. (More about the competing dynamical process under the electron beam in the following sections).

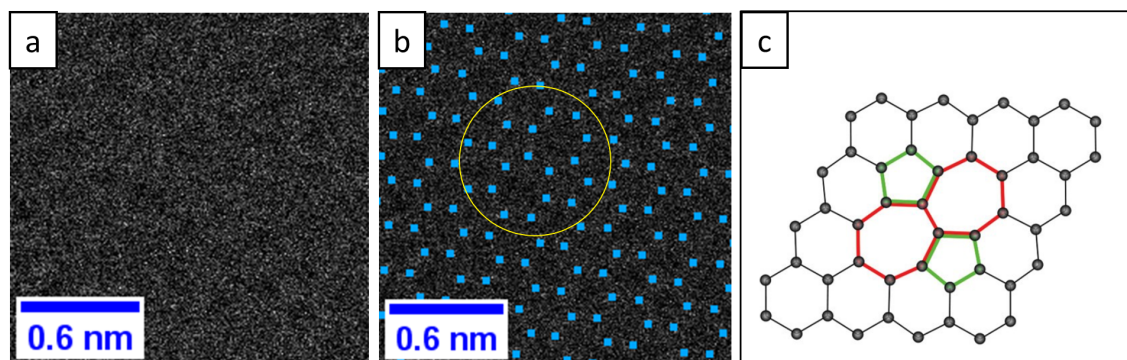


Figure 1.3: Stone-Wales defect in graphene. (a) A raw image of a SW(55-77) defect observed during our atom manipulation experiment. (b) An overlay identifying the atoms location using the structure recognition integrated into the Nion Swift Atom Manipulator plug-in, where the SW defect can be clearly seen. (c) A simulated SW(55-77) defect (adapted with permission from Ref. [16]. Copyright 2011 American Chemical Society.)

1.3.3 Substitutional impurities and carbon adatoms

A substitutional defect is formed in graphene when a foreign atom replaces an original carbon atom in the graphene lattice and takes over its lattice site. Heteroatoms doping in graphene can be of great advantage, not only for enhancing its electronic properties by opening a band gap, but also for tailoring its mechanical and chemical properties [5]. Heteroatoms doping has been achieved using various methods ranging from chemical doping [26] and the use of molecular precursors [27] to utilizing two-step deposition process [28] and the ultralow-energy ion implantation method [29].

Due to their proximity to carbon in the periodic table, early work on incorporating heteroatoms in graphene was mainly conducted on boron (B) and nitrogen (N) leading to *p*-type and *n*-type doping respectively [30, 31]. Many transition metals (TMs) have since been observed or deliberately introduced into a single layer of graphene: gold (Au) with potential for graphene spintronics applications [32], iron (Fe) [33] and manganese (Mn) [34] for investigating magnetic functionality, in addition to other TMs such as platinum (Pt) [35] and chromium (Cr) [33]. When an impurity heavier than N is doped into graphene, it buckles out of the plane when incorporated into a single vacancy. This is because they have large covalent radii compared to carbon, thus they form longer bonds with the three neighbouring carbon atoms compared with the bond length between carbon atoms in graphene. When replacing two carbon atoms by occupying a larger DV [16], most impurities lie in the graphene plane.

Many impurities show interesting dynamical behaviour under electron irradiation [9]. Some of the impurities have been predicted or observed to be manipulable under electron irradiation including P [36], N, B, Fe, Si and Al [10].

Silicon (Si) impurities are of great relevance to this work since manipulating and testing automated atom manipulation is easiest on Si impurities in graphene. Si impurities have been reported to move in the graphene lattice in a controlled way by manually parking the STEM electron beam on a carbon neighbour [7]. Si impurities are observed in almost all graphene samples synthesised by chemical vapour deposition (CVD) or prepared by thermal decomposition of SiC compounds. Si impurities bind with three carbon atoms in a SV and buckle out of plane in a mostly sp^2 hybridized form denoted as (Si-C₃) [23], while when bound with four carbon atoms in a DV they form in-plane sp^2d like hybridization [37] denoted as (Si-C₄); in general this notation will be used for any dopant atom as (X-C₃) and (X-C₄) respectively, where X is the chemical symbol of the dopant. Figure 1.4 shows a Si impurity atom in graphene with 4-fold coordination.

The other part of this thesis was to deposit Al impurities into a single layer of graphene and investigate their behaviour under the electron irradiation of STEM. The dynamics of single Al impurities in graphene have been recently studied and it was predicted to be a promising candidate for atom manipulation [10].

1 Introduction

Due to the high energy cost, interstitial atoms never exist in graphene. Therefore any additional diffused carbon atoms will lay over the planer lattice structure, where the bridge between two carbon atoms is the energetically favoured location for a carbon adatom. The carbon adatom at this position have a different hybridization to that of the two surface atoms it is attached to, which have sp^2 - sp^3 hybridization [38]. The binding energy in this bridge site is between 1.5 to 2 eV [16]. The presence of carbon adatoms on graphene is not desirable for single atom manipulation, because they might replace the impurity during the manipulation process [23].

Samples with Si impurities were already prepared by colleagues. For incorporating Al impurities into graphene lattice, we had to use in-situ physical vapour deposition, where an evaporator is in the same vacuum system connected to the Nion UltraSTEM 100. I will give more details about the Al heteroatom deposition in graphene in the experimental methods section.

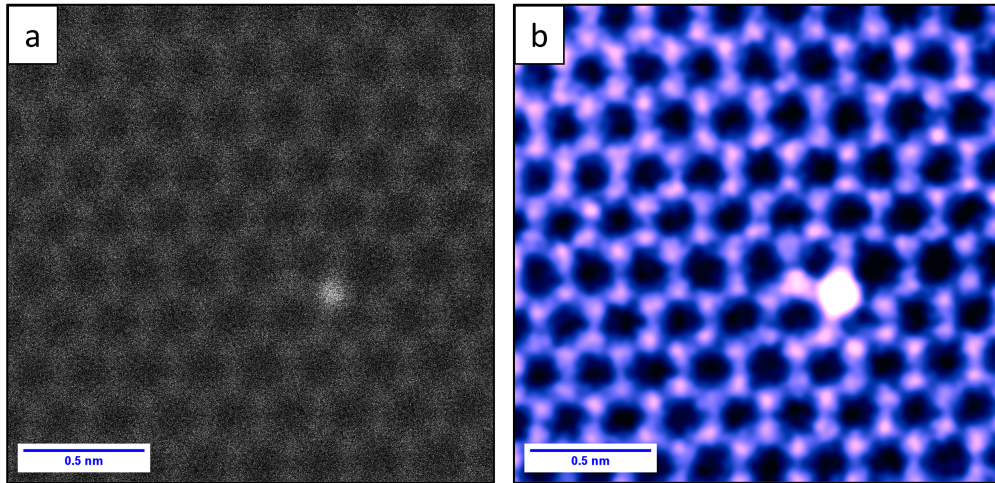


Figure 1.4: Si heteroatom in graphene. a) A raw dark field image of a four-fold (Si-C_4) single silicon atom in graphene lattice with a field of view (FOV) of $2 \times 2 \text{ nm}^2$ recorded by a medium angle annular dark field (MAADF) detector using the Nion UltraSTEM 100 at 60 keV with 1024×1024 px. b) A colored version of the same image after being processed using a double-Gaussian filter. The scale bar was added with ImageJ by using the scale in the meta data of the raw image.

1.4 Diffusion of defects

The main driving force of diffusion in any solid system is to minimize Gibbs free energy [39]. The temperature dependence of diffusivity D in solids obeys Arrhenius's law [40]

$$D = D_0 \exp\left(-\frac{Q}{k_B T}\right), \quad (1.4)$$

where D_0 is a pre-exponential factor, Q is the activation enthalpy of diffusion (referred to also as the migration energy), k_B is Boltzmann constant and T is the absolute temperature. This temperature dependency applies for the diffusion of vacancies, substitutional atoms and adatoms on graphene surface.

Different defect types diffuse in graphene following different mechanism. SW (55-77) defects diffuse by iterated SW rotations [24]. A SV can migrate in graphene to a neighboring atomic site if provided with the required migration energy calculated to be ca. 1.3 eV, much lower than the estimated experimental value of 3.1 eV in graphite [21]. Unlike single vacancies that can migrate slightly above room temperature, DVs have much larger activation energy of ca. 7 eV, making them immobile up to very high temperatures [16]. These immobile DVs act as nucleation sites for migrating SVs and can form complex vacancy structures [20]. Diffusion of substitutional atoms usually occurs by a vacancy mechanism, in which the impurity jumps to an adjacent vacant site when supplied the required migration energy [39]. Substitutional impurities in graphene are very stable due to the covalent bonds they form with the carbon, but their diffusivity can be enhanced when under irradiation [41]. Actually many thermally prohibited dynamics can be activated by energetic electron irradiation.

Regarding single atom manipulation, diffusion of adatoms on graphene surface is a relevant competing process since they can replace the targeted impurity atom during the manipulation under the electron beam. Adatoms diffusion can be induced by a gradient in the chemical potential at high coverage of the diffused species or as a spontaneous jumps of the particles in the absence of such a gradient (low coverage) [23]. Carbon adatoms diffuse on graphene from site to site by overcoming an energy barrier E_{diff} each time. When $E_{\text{diff}} \gg k_B T$ the carbon adatoms diffuse by hopping mechanism and the hopping frequency ν can be obtained from the relation [42]

$$\nu = \nu_0 \exp\left(-\frac{E_{\text{diff}}}{k_B T}\right), \quad (1.5)$$

where ν_0 is oscillation of the carbon atom around it's equilibrium position. The calculated migration barrier for carbon adatoms on a flat graphene surface is about 0.4 eV, which is why it is not possible to observe them using TEM or STEM even at room temperature [16].

1.5 Irradiation effect of energetic electrons in graphene

In a transmission electron microscope, imaging is performed using highly accelerated electrons that can interact with the material in various ways. Insulators for example can be readily ionized and damaged by fast electrons due to bond breaking, while metals can neutralize inelastic interactions due to their free conduction electrons. Graphene behaves as a metal under irradiation due to its high charge carrier mobility and thus pristine graphene is not susceptible to ionization damage [43]. When the electron beam hits the graphene sample, one can distinguish between two type of interactions:

- Electron-electron inelastic scattering: can lead to various kind of excitations ranging from phonon and plasmon up to core level excitations. This is useful for characterizing the sample using spectroscopic measurements such as electron energy-loss spectroscopy (EELS) and energy dispersive X-rays (EDX) spectroscopy. In this work we used EELS for identifying single-atom impurities in the graphene lattice.
- Electron-nucleus elastic scattering: can lead to interesting topological and structural changes in the local structure, which forms the basis for this work. The knock-on process resulting from the electron-nucleus interaction will be discussed in more detail in the next sections.

1.5.1 Knock-on damage of carbon atoms

Knock-on damage in the scope of this work is the elastic collision between a beam electron and a carbon atom leading to its ejection out of the lattice [44]. In order for this process to happen, a minimum amount of kinetic energy must be transferred to the carbon nucleus target, referred to as the displacement threshold energy E_d . The threshold energy required to remove one carbon atom in pristine graphene is about 21 eV. Despite the fact that in a STEM we use electrons energies up to 100 keV, the energy transferred to a carbon atom is only on the order of a few eV due to the small mass of the electrons compared with the carbon nucleus (ca. 2200 times smaller) [45].

In the following I will give a brief mathematical description of the transferred energy during the collision between the relativistic accelerated electrons and the nucleus followed by a discussion of the temperature dependency of the displacement threshold energy.

1.5.1.1 Energy transfer in the static-nucleus approximation

The relativistic momentum of an electron is related to its kinetic energy E_e as $p_e = \frac{1}{c}\sqrt{E_e(E_e + 2E_0)}$, where c is the speed of light, E_e in a STEM is equal to $E_e = eU$ (U is the accelerating voltage) and $E_0 = m_0c^2$ is the electron rest energy. During an elastic scattering of a relativistic electron from a nucleus, both the total momentum and energy of the system are conserved. Applying these conservation relations and taking into consideration that the energy transfer E'_n is very small compared with the incoming

electron kinetic energy, the energy transferred to the nucleus is

$$E'_n = \frac{2}{Mc^2} E_e (E_e + 2E_0) \sin^2\left(\frac{\theta}{2}\right), \quad (1.6)$$

where M is the mass of the nucleus and can be written as a function of the mass number A of the target atom: $M = Am_u$, and m_u is the atomic mass unit (a detailed derivation can be found in [46]). A maximum energy transfer E_{\max} to the nucleus can be reached in the case of head-on collision, in which the electron is backscattered ($\theta = \pi$) and can be written in the form [47]

$$E_{\max}(\text{eV}) = \frac{2148}{A} E_e (E_e + 1.02), \quad (1.7)$$

where E_e and E_0 are in MeV. This equation shows us that that transferred energy depend on the speed of the incoming electron and the mass of the target atom. more energy can be transferred to lighter elements.

1.5.1.2 Energy transfer considering lattice vibration

An enhanced model for describing the transferred energy was suggested by Mayer, Kotakoski and others, which takes lattice vibration into account. Despite the fact that the vibration energy (on the order of meV) is very small compared to the energy of the incoming electrons, the movement of the target atom can significantly increase the transferred energy that it can receive [48]. When taking the movement of the nucleus before collision into account, the conservation of momentum $\vec{p}_e + \vec{p}_n = \vec{p}'_e + \vec{p}'_n$ gives us when taking the projection onto the horizontal axis:

$$p_e + p_n \cos \alpha = p'_e \cos \theta + p'_n \cos \varphi, \quad (1.8)$$

and the conservation of energy $E_e + E_n = E'_e + E'_n$ gives:

$$E'_e = E_e + E_n - E'_n \quad (1.9)$$

The maximum transferred energy can be obtained when the nucleus with velocity v is moving parallel to the incoming electron ($\alpha = 0$) and treating only the head-on collision case ($\theta = \pi$), which leads to a scattering angle of the nucleus of $\varphi = 0$, thus giving

$$p'_n = p_e + p_n + p'_e. \quad (1.10)$$

Since the energy of the incoming electron is much higher than the energy of the nucleus after or before collision ($E_e \gg E_n, E'_n$), one can approximate the relativistic momentum of the scattered electron using $E'_e = E_e + E_n - E'_n \approx E_e$ as

$$p'_e = \frac{1}{c} \sqrt{E'_e(E'_e + 2E_0)} = \frac{1}{c} \sqrt{E_e(E_e + 2E_0)} \approx p_e. \quad (1.11)$$

Thus equation (1.10) becomes

$$p'_n = 2p_e + p_n. \quad (1.12)$$

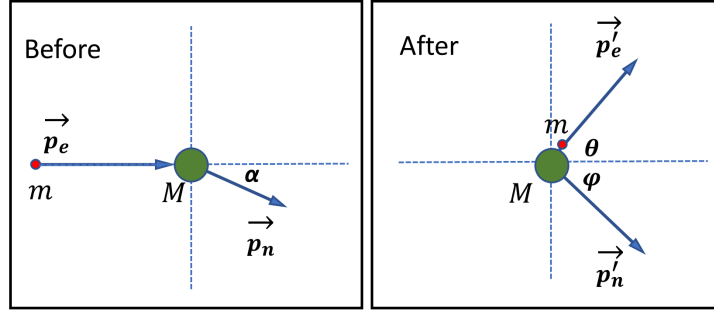


Figure 1.5: Schematic illustration of elastic scattering of an energetic electron with mass m with the nucleus of a target atom of mass M .

Using a non-relativistic expression for the momentum for the nucleus before the collision, $p_n = \sqrt{2ME_n} = Mv$, and after the collision, $p'_n = \sqrt{2ME'_n}$, we get an analytical expression of the maximum transferred energy of the nucleus as

$$E_{\max} = E'_n = \frac{1}{2Mc^2} \left(Mvc + 2\sqrt{E_e(E_e + 2E_0)} \right)^2. \quad (1.13)$$

The statistical distribution of the atomic velocities perpendicular to the lattice plane can be described by the temperature-dependent mean square velocity $\overline{v_z^2}(T)$, which can be calculated using the out-of-plane phonon density of states $g_z(w)$ [45]:

$$\overline{v_z^2}(T) = \frac{\hbar}{2M} \int_0^{w_z} g_z(w) \left(\frac{1}{2} + \frac{1}{e^{\frac{\hbar w}{kT}} - 1} \right) w dw, \quad (1.14)$$

where \hbar is the reduced Plank constant, k is Boltzmann constant, T is the temperature in Kelvin and w_z is the highest out-of-plane lattice vibration frequency. The calculated temperature-dependent root mean square velocity $v_{\text{rms}}(T)$ at room temperature is equal to $v_{\text{rms}}(300 \text{ K}) = \sqrt{\overline{v_z^2}(300 \text{ K})} \approx 560 \text{ ms}^{-1}$ [23]. Subsequently we can see from relation (1.13) that when taking lattice vibration into account, the maximum transferred energy is shifted upwards compared with the static nucleus approximation., which is shown in figure 1.6 for the case of an initial velocity of the target atom of $v = 3v_{\text{rms}}(300 \text{ K})$.

The displacement threshold energy was further found to have a finite spread following a symmetric distribution when investigated using a density-functional tight-binding (DFTB)-based MD [49]. It was found that the full width at half maximum (FWHM) increases with increasing the temperature until it reaches a constant value at room temperature ($T = 300 \text{ K}$). This spread in E_d values with changing temperature could not be explained by the movement of the target C atom itself, but by the relative motion of the target atom with respect to its three carbon neighbours. When the neighbour atoms are moving in the opposite direction relative to the target atom, the energy required to knock it out of the lattice decreases, while it's more difficult to knock it out when the neighbour atoms are moving in the same direction, and thus a higher transferred energy is needed.

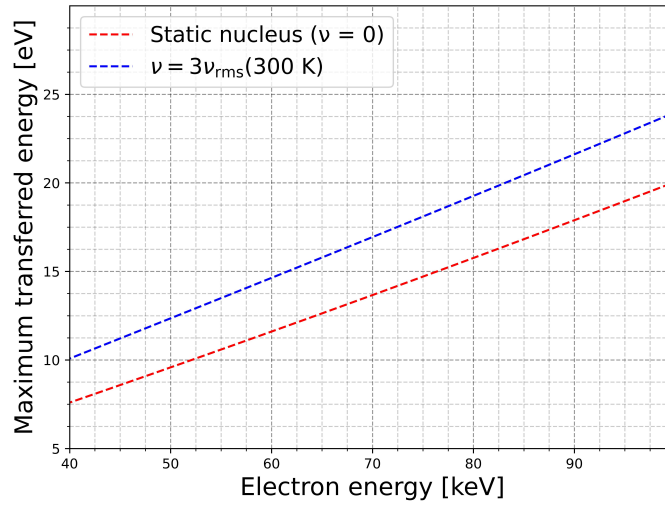


Figure 1.6: Maximum transferred energy E_{\max} as a function of the electron energy in keV. The plot shows that E_{\max} is larger when considering the movement of the nucleus before collision (blue dashed line) compared with the static nucleus case (red dashed line). (Adapted with permission from Ref. [23].)

1.5.2 Knock-on displacement of impurity atoms

The presence of single impurity dopants in the graphene lattice is necessary for the purposes of this work, thus understanding the effects dynamics of doped graphene under the electron beam in a STEM must be considered. Si and Al dopants have lower displacement threshold energies compared to carbon, but due to their larger mass, the displacement cross section for these dopants is much smaller. Thus removing Si or Al dopants leaving behind a vacant site in the graphene sheet is less likely to occur and was rarely observed [23], which is good for the purpose of single atom manipulation since we do not want to lose the atom we aim to manipulate (Removing the dopant atom leaving behind a vacancy was however sometimes observed during my experiment on Al manipulation). When the impurity atom is knocked out of the lattice a migrating carbon adatom can take over the left behind vacant lattice site recovering a locally pristine graphene structure when no other dopants are present.

1.6 Impurity atom manipulation in graphene

In recent years, single-atom manipulation using a STEM has emerged as a cutting-edge research tool in the field of 2D nanostructured materials. The ability of precisely positioning and arranging individual atom in a certain design opens the door to the highest level of material engineering. The focused and energetic electron probe facilitates the manipulation process, in which it is aimed at one of the carbon neighbours of the impurity atom to induce a swapping of position between it and the targeted carbon atom.

1 Introduction

There are two mechanism by which this can occur: either by direct exchange (also known as the X-C bond inversion [23, 8], where X refers to the impurity atom), or via a SW bond rotation. In both of these processes the number of atoms is conserved. On the other hand, the electron beam can also induce two undesired effects: knocking out the impurity atom from the lattice, or knocking out the target carbon atom. In this section I will briefly describe these competing effects.

1.6.1 Direct exchange

It was discovered in 2014 by Toma Susi and colleagues that single Si atoms in graphene show an intriguing behaviour when under electron irradiation in a STEM, in which they move through the lattice without any structural damage [8]. Using first-principles molecular dynamics simulations it was shown that these jumps are due to a swapping of positions between the Si atom and its carbon atom neighbour in a process called Si-C bond inversion, later renamed as direct exchange.

In the direct exchange process, a single electron impacts one of the neighboring carbon atoms of the impurity atom. When the energy transferred to the target carbon atom is in a certain range below the knock-on damage threshold energy, this will lead to displacing the carbon atom out of the graphene plane but not being removed totally, while in the same time the impurity atom relaxes to the vacant site left by the displaced carbon atom, after which the carbon, due to the interaction with the dopant atom, relaxes back to the graphene lattice occupying the original lattice site of the dopant. The carbon atom involved in this process is referred to as the primary knock-on atom (PKA). It should be noted that this process is only valid for a three-fold impurity atom ($X-C_3$) due to their nonplanarity, while it is not possible to manipulate a four-fold impurity atom ($X-C_4$), largely because it lies in the same plane as the neighboring four carbon atoms.

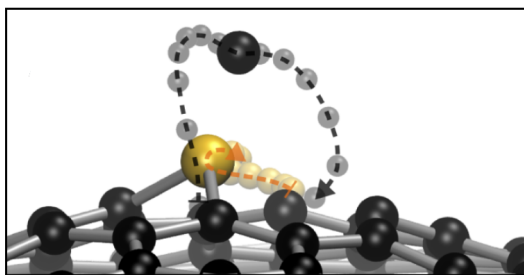


Figure 1.7: An illustration of the direct exchange process by molecular dynamic simulation. In this process, the three-fold Si atom (shown in yellow) relaxes to the vacant site left by the displaced C neighbor. The C atom is attracted back to the lattice to take the original site of the Si impurity resulting in a position exchange between the two atoms (Adapted from Ref. [8].)

1.6.2 Stone-Wales rotation

A SW transformation (hexagonal to the metastable configuration 55-77) followed by another SW rotation (from the metastable 55-77 configuration back to the hexagonal one) is equivalent to a direct exchange process between the impurity atom and a neighbouring carbon atom [23] when both rotations occur in the same direction. Thus some of the jumps the impurity atom performs under the electron beam in STEM may be ascribed SW transitions, making them a desirable induced effect in the scope of single-atom manipulation. Among the different induced processes under electron irradiation, the SW transformation can have the largest cross section [9]. However, it is usually not observable due to the very short timescale it happens on and the fact that the scanning by the electron beam is not continuous [9].

1.6.3 Replacement of dopants by C adatoms

The process of removing the dopant under the electron beam or replacing it by a C adatom, which was described in section 1.5.2. This induced effect is undesired during single-atom manipulation.

1.6.4 Ejection of one of the neighboring C atoms

By removing the PKA from the lattice under electron irradiation, the three-fold impurity atom ($X-C_3$) turns into a four-fold one ($X-C_4$). This can be described as a trap state [9], since once it is reached, the impurity atom cannot be manipulated anymore as has been observed by previous colleagues and predicted by theory. Turning the dopant into a 4-fold atom is considered a main limiting process for single atom manipulation.

2 Methods

2.1 Scanning transmission electron microscopy

This section is based for the most part on the transmission electron microscopy book of William and Carter [50]. Due to the fundamental physical limitation for imaging with light represented by its wavelength known as Abbe's diffraction limit, acquiring atomically resolved images was only possible after the rise of electron microscopy. Abbe's idea shows that it's not possible to resolve distances much smaller than the wavelength being used. Electron microscopy arose as a beautiful manifestation of the electron particle-wave duality suggested by de Broglie. Accelerated electrons with energies of several tens of eV have a wavelength on the order of a few pm, which is small compared with atomic distances, so achieving atomic resolution in electron microscopy is instrumentally limited by the imperfections in the lens system rather than being physically limited the electron's wavelength itself.

In contrast to TEM where a coherent parallel beam is used for acquiring images and diffraction patterns, STEM uses a convergent incoherent beam that is scanned over the sample. An electron gun is used in STEM to produce an electron beam with a high brightness. Most modern instruments have a field emission gun (FEG), in which there are two anodes: first one for extracting the electrons from the cathode tip and the second anode used to accelerate them. For this we need an ultra-high vacuum (UHV) conditions, otherwise contamination will disrupt the tunneling process of the electrons out of the tip.

The combination of the positive anodes allows to form a cross-over of the electron beam, which acts as an object for the first lens in the illumination system. The condenser lenses in the illumination system form a sharp electron beam which is scanned over the sample.

The electrons transmitted through the sample can be picked up by different detectors after passing the last projector lens. For detecting the electrons the most common detectors can be categorized in two kinds. The first one uses a scintillator that emits visible light when hit by electrons and which is coupled to a photomultiplier tube (PMT). The second way is using a semiconductor detector based on a Si pn-junction, in which electrons are excited from the valence band to the conduction band forming electron-hole pairs in the silicon when the detector is hit by the energetic electrons. Semiconductor detectors are highly responsive to electrons and robust when it comes to radiation damage, but they have a smaller bandwidth and higher noise level when compared to the

scintillator detectors in the MHz range. In general, scintillator detectors are preferred in electron-microscopic devices. Charge coupled device (CCD) detectors based on stored charges when hit by electrons are also used in S(TEM) instruments, but regular CCD detectors cannot handle the energetic electrons and are quite expensive. Most STEM devices have EELS detector for elemental and chemical characterization of the sample for which a magnetic prism is placed after the EELS entrance for dispersing the signal (more about the EELS in the section).

2.1.1 STEM imaging system

Image formation in STEM is based on forming a very sharp probe that is scanned over the sample in a raster using scanning coils such that the beam remains parallel to the optical axis during the scanning. Thus both the resolution and the quality of the image are defined by the electron probe. To obtain such a highly focused beam the first condenser lens (C1) should strongly focus the beam, so much so that most of the electrons coming from the electron gun are not focused on the second condenser lens (C2) and are simply lost. The aberrations that can limit the image quality are basically related to the aberration in the electron probe itself, and since the condenser lenses are used to form the sharp electron probe in STEM, their aberrations are the main limiting factor of the image resolution. For this reason, many modern STEM devices are provided with an additional condenser lens (C3) with an aberration corrector system [50].

For single-atom manipulation having a very sharp electron beam that is precisely directed on the target atom is very important. The spatial distribution of the electron beam perpendicular to the probe axis is thus an important factor [23], especially for quantitative analysis of the electrons hitting the sample. The shape of the electron beam can be described by a combination of Gaussian line shapes [23].

2.1.2 Annular dark field detection

All images taken during this project were acquired using a medium angle annular dark field (MAADF) detector. Unlike dark field (DF) images in TEM where the contrast comes from a fraction of the coherently scattered electrons (Bragg), DF STEM images are formed by collecting most of the incoherently scattered electrons on the ADF detector (Rutherford) [50].

The signal detected by an ADF detector depends mainly on the atomic number Z and thickness of the sample. Thus for graphene and similar 2D materials, the signal depends only on Z , therefore it is called Z -contrast. Thus ADF imaging is very useful for defining the local atomic structure [51] and identifying defects and heteroatoms incorporated into graphene by distinguishing between them and carbon atoms from their brightness: the heavier the atom the brighter it looks in an ADF image.

2.1.3 Nion UltraSTEM 100

The primary instrument used in this project was the Nion UltraSTEM 100 located at the Sternwarte facility in Vienna. Figure 2.1 shows the Nion UltraSTEM 100 with a diagram illustrating the main parts of the instrument. It was used to obtain atomically resolved images of impurity atoms embedded in graphene, as well as to characterize these single-atom impurities using EELS and eventually to manipulate them using a software plugin developed by our colleague Andreas Postl, which was installed on the Nion Swift software provided by the manufacturing company.

Nion UltraSTEM 100 [52] is provided with a cold field emission gun (CFEG) with an accelerating voltage up to 100 kV with a beam current of ca. 50 pA. Our atom manipulation experiments were always conducted at an accelerating energy of 60 keV. The electron gun is placed at the bottom of the STEM to ensure mechanical stability and it was kept under ultra-high vacuum conditions with pressure of about 10^{-11} Torr. The small probe diameter of about 1.2 Å is an essential factor for the purposes of atom manipulation. During the experiment, the MAADF detector was mainly used for both imaging

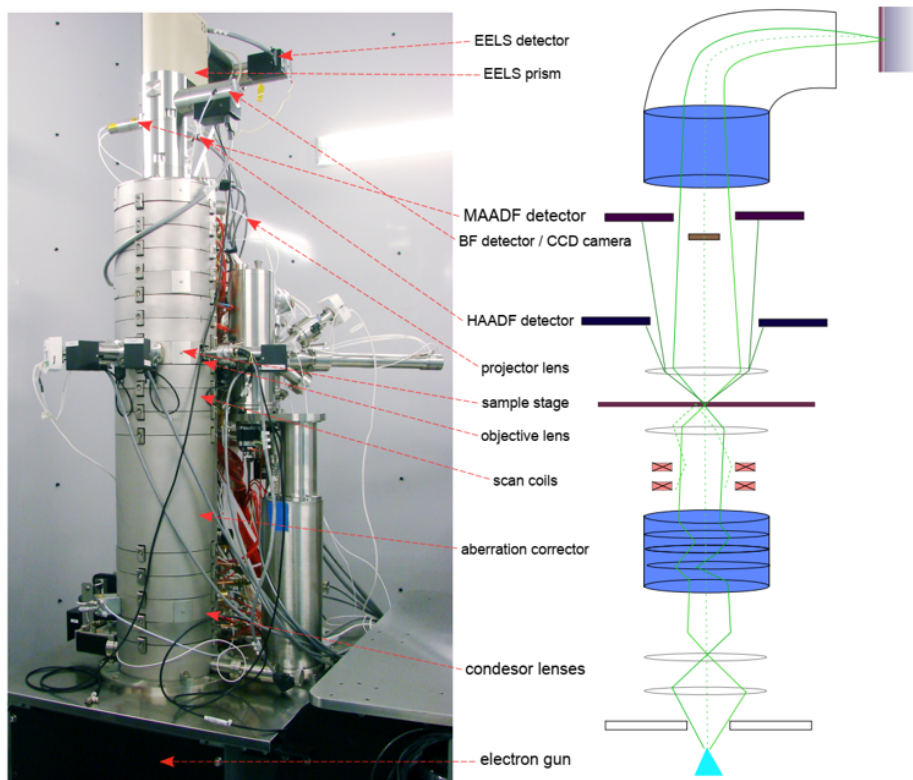


Figure 2.1: The Nion UltraSTEM 100 in Vienna with a schematic illustration of its components. (Adapted from Ref. [51].)

and manipulations. The average maximum intensity of the MAADF detector increases with the atomic number of the imaged material as $Z^{1.64}$ (Z -contrast) [23]. Nion UltraSTEM 100 is also provided with an EELS detector that helps with material characterization.

One of the key advantages of the Nion UltraSTEM 100, aside from its aberration correction system, is that it is fully computer-controlled. The instrument is isolated in a separate room and operated entirely remotely. There are two main software applications for operating the STEM: the Nion AS2 and the Nion Swift. For microscopy and spectroscopic measurements, users exclusively work with the latter. Nion Swift is an open-source application with an application programming interface (API) that allows users to customize it according to their specific needs. This software feature is essential, as it enabled the customization of Nion Swift by adding a plugin for automated manipulation [23].

2.2 Electron energy-loss spectroscopy

High-energy electrons in a STEM can interact with the atoms of the target material through Coulomb forces in various ways. As explained in the previous chapter, electrons undergo elastic scattering when they interact with the atomic nuclei of the sample. However, when fast electrons interact with the electrons of the sample through Coulomb interactions, they undergo inelastic scattering. During this process, the primary beam electrons lose a small part of their energy, resulting in scattering at small angles of a few milliradians [53].

EELS is an analytical technique based on measuring the energy loss distribution of these inelastically scattered electrons [54]. This is accomplished using a magnetic prism spectrometer that bends and disperses the electrons based on their energy loss. The radius of the circular path the electrons follow inside the magnet is directly dependent on their energy loss and is given by

$$R = \left(\frac{\gamma m_0}{eB} \right) v, \quad (2.1)$$

where $\gamma = (1 - \frac{v^2}{c^2})^{-\frac{1}{2}}$ and v represents the velocity of the inelastically scattered electrons that enter the magnetic prism perpendicular to the applied magnetic field B . Subsequently, the magnetic prism focuses the electron beam after it exits the magnet, allowing it to be collected by the detector [53]. Equation 2.1 shows that electrons experiencing higher energy loss have smaller velocities and are consequently bent more than electrons with smaller energy losses.

The inelastic cross section of the electron-electron interaction depends on the kinetic energy T of the beam electron. The lower the kinetic energy the larger the cross section of the energy loss process. This is attributed to the fact that lower energy electrons pass slower through the specimen, thus they have more time to interact with the atomic

2 Methods

electrons. Furthermore, the inelastic cross section depends on the energy-loss E of the primary beam electrons. The higher the energy loss the closer the atomic electrons to the nucleus and the lower the cross section of the process, since the inner shell electrons occupy less space around the nucleus. This can be shown from the equation that gives the double differential inelastic cross section [55]

$$\frac{d\sigma_i^2}{d\Omega dE} = \frac{4a_0^2 R^2}{T} \frac{1}{E} \frac{df}{dE} (\theta^2 + \theta_E^2)^{-1}, \quad (2.2)$$

where R is Rydberg constant, a_0 is Bohr radius, θ is the scattering angle, $\theta_E = \frac{T}{2E}$ is the characteristic scattering angle and $\frac{df}{dE}$ is the optical oscillator strength.

The EEL spectrum is rich in information and is useful for elemental characterization, probing the valence band, defining the band gap, and assessing sample thickness [50]. It can also provide detailed insights into the bonding between atoms in the specimen [56]. The EEL spectrum can be divided into three distinct regions, each offering different information about the sample:

- The zero-loss peak (ZLP) is the most prominent feature of the EEL spectrum. It consists of electrons transmitted without any energy loss, elastically forward scattered electrons, and electrons that caused phonon excitations that cannot be resolved [53]. The full width at half maximum (FWHM) of the ZLP corresponds to the energy resolution of the instrument [50].
- The low-loss region, ranges from approximately 5 to 50 eV and primarily includes excitations of the outer-shell electrons. The plasmon peak is relatively intense and forms the background of the high-loss region. The fine structure of the low-loss region can provide valuable information about the valence band and the electronic structure of the sample [53].
- The high-loss region within the EEL spectrum has lower intensity compared to the previous ones due to the decrease in the inelastic cross section with increasing energy loss. This region provides valuable information about the elemental composition of the sample by probing the excitations of inner-shell electrons. The onset of each core-loss peak in the high-loss region of the EEL spectrum is called the core ionization edge, because they have a sharp edge at the ionization threshold [53].

In this thesis, we are mainly interested in the core-loss features, which we used for identifying the single Al and Si impurities deposited in our graphene sample. The EEL spectra were acquired using the EEL spectrometer (PEELS 666, Gatan Inc.) installed in the Nion UltraSTEM 100 at Sternwarte. The spectrometer is connected to an electron-multiplying CCD camera, namely the iXon Ultra897 by Andor. The L -edge of Al lies at 73 eV. This consists of two overlapping features: the L_2 which arises from the $2P_{1/2}$ and the L_3 edge corresponding to $2P_{3/2}$. Occasionally we have also measured the EEL spectrum of Si single atoms to distinguish them from the Al impurities, but this was not necessary when using a graphene sample with only Si impurities. The L -edge onset of Si lies at about 99 eV.

2.3 Low-energy ions for defect engineering

Incorporating defects in 2D materials has emerged as a powerful approach for tailoring their properties, making defect engineering a main focus for many research groups. It has been demonstrated that charged particles like electrons or ions can be of a great advantage for modifying the structure and properties of 2D materials [57]. This is mainly achieved through momentum or energy transfer from the charged particles to the nanostructure system. Elastic interactions result in knock-on displacement, while inelastic interactions lead to ionization damage (radiolysis) of the material [51].

To manipulate atoms in graphene, it was necessary to introduce single-atom impurities into the lattice. Using low-energy ion irradiation is convenient for this purpose since the defects induced in 2D materials are point-like defects [58], which can host single-atom impurities. When an ion collides with a target atom, it scatters due to the screened Coulomb potential. During the scattering process, the ion transfers kinetic energy to the target through momentum transfer. The maximum transferred energy in the case of a static target atom is given by [59]

$$E_{T,\max} = \frac{4m_1m_2}{(m_1 + m_2)^2} E_k, \quad (2.3)$$

where E_k is the ion kinetic energy. The differential cross-section that describes the transferred energy E_T during this elastic scattering (where energy is transferred into kinetic energy and not into exciting the internal degrees of freedom of the system) can be described by Thompson's formula

$$\sigma(E_T) = \frac{m_1}{m_2} \frac{\pi(Z_1 Z_2 e^2)^2}{E_{k,1} E_T^2}, \quad (2.4)$$

where Z_1 and Z_2 refer to the atomic number of the ion and the target atom, respectively. From this relation, we can see that the probability of an ion with mass m_1 to transfer energy E_T to a target atom with mass m_2 increases with their mass ratio and decreases with increasing the ion kinetic energy. Furthermore, it decreases even more rapidly for higher transferred energies. The elastic scattering process is commonly known as nuclear stopping since it takes place between the ion and an atom target of the material [58]. The energy deposited in the system in this case can be described by the energy loss per unit length

$$S_n = -\frac{dE_n}{dx}. \quad (2.5)$$

As it is shown from equation 2.4, in the case of high-energy ions, the nuclear stopping become irrelevant. The ions in this case will interact mainly with the electronic system of the material causing electronic excitation or even ionization damage to the material. This is referred to as electronic stopping, but it is not relevant to this thesis.

2.4 Sample preparation

2.4.1 TEM grids and graphene films

During this project, commercial monolayer (ML) graphene films (Graphenea)-easy transfer synthesized using chemical vapor deposition (CVD) using poly(methyl methacrylate) (PMMA) as a support were used [60]. These films were used for both samples: those with Si dopants as well as those with Al dopants. The sample with Si impurities was already prepared by colleagues and was loaded in the vacuum system connected to the STEM. It was supported on a thin perforated silicon nitride grid SiN/Si (Silson Si3N4-TEM) with a membrane thickness of 50 nm and one window that has evenly distributed holes of 2.5 μm in diameter for TEM imaging. The membrane was supported on a thin Si substrate [23].

The graphene samples onto which Al impurities were deposited were prepared by myself with the help of colleagues in the group. The graphene ML was transferred onto a thick SiN/Si grid (Silson SiRN-TEM) with membrane thickness of 1000 nm with 3×3 windows each of size of $0.09\times 0.09\text{ mm}^2$ and a frame thickness of 200 μm . The thick SiN/Si grid had 9 windows, each containing 23 to 25 holes for imaging.

2.4.2 Graphene transfer and removing PMMA

To transfer the graphene ML onto the plasma-cleaned TEM grid, we initially cut a small piece from the Graphenea film and placed it in deionized water, allowing it to float. Then the grid was carefully positioned underneath the floating graphene ML using reverse tweezers for capturing it and removing the assembly from the deionized water. Following a drying process, we placed the sample on a hot plate at 150°C for one hour to enhance the adhesion between the graphene ML and the grid substrate.

Afterward, we proceeded with vacuum annealing of the sample in a Mantis Hex deposition system to soften the PMMA layer before dissolving it by solvent [60]. This was done by placing the sample directly onto a tungsten boat, which was connected to the sample stage. It was then inserted into the Mantis Hex chamber and heated to 550°C for one hour, using a current of 11 A, under a vacuum condition of 10^{-6} mbar. The temperature was read by attaching a thermocouple to the tungsten boat.

Following the vacuum annealing, the sample was treated with hot acetone solvent at 50°C for one hour. To remove any residual solvent, the sample was subsequently immersed in isopropanol alcohol for one hour. The grid then was transported to the laboratory in Sternwarte in Vienna where the STEM is located and was inserted in the vacuum system there.

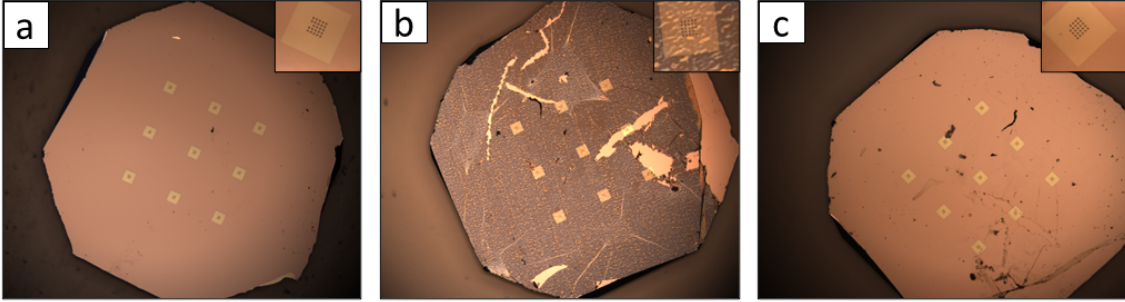


Figure 2.2: Optical microscope images with $5\times$ magnification of the thick Silson SiRN-TEM grid used for depositing Al impurities on graphene during different stages of sample preparation. The inset in the top right corner of each image shows images of a single window at $100\times$ magnification. a) The plasma-cleaned grid before transferring the graphene ML onto it. b) The grid after the transfer of the graphene ML with the PMMA. c) The grid after removing the PMMA layer using both annealing and hot acetone bath. The graphene ML is left on the grid.

2.5 In situ sample processing

One of the key features of the STEM at Sternwarte in Vienna is its connection to a UHV transfer system that spans over two floors and includes various devices for sample processing. The UHV-assembly, including the Nion UltraSTEM 100, is called CANVAS system as depicted in Figure 2.3, which is an acronym for Controlled Alteration of Nanomaterials in Vacuum at the Atomic Scale [61].

The CANVAS system has the capacity to store up to 72 samples, each mounted on a sample holder called a puck and inserted into wheeled transfer vehicles called cars. Each car has space for three pucks and can be transported inside the UHV system using magnetic coupling.

For brevity I will mention only the devices needed for preparing the sample and conducting the atom manipulation experiment (a detailed description of the set up can be found in Ref. [61]). For forming vacancies in the graphene sample, we used a plasma source SPECS MPS-ECR mounted in the so-called target chamber. The chamber is equipped also with a 6W 445 nm-wavelength diode laser that we used for both cleaning the sample and healing nanopores and vacancies within it. To introduce Al impurities into the sample, we used a vacuum thermal evaporation (VTE) source RIBER S40 for the physical vapor deposition (PVD) process. The Nion UltraSTEM 100 is equipped with a column laser unit that have been occasionally also used during our experiment. In the following sections I will describe these techniques in more details.

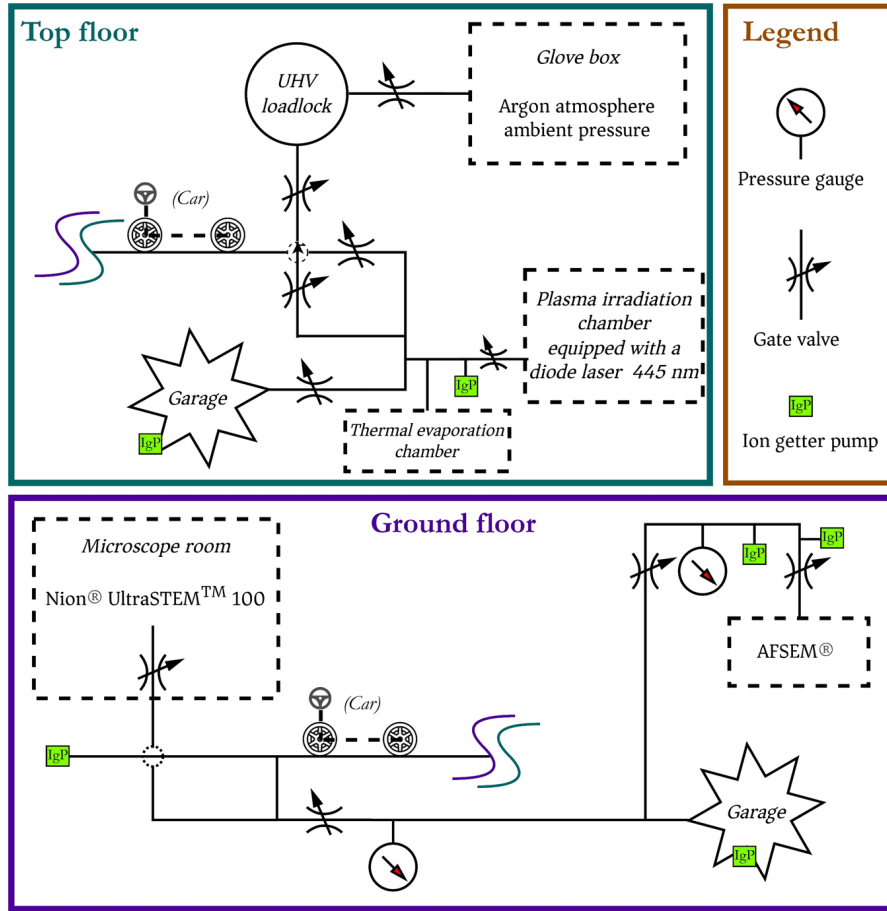


Figure 2.3: Schematic of the UHV system installed at Sternwarte in Vienna. Samples are loaded onto pucks, which are transported through the system using cars via magnetic coupling. Each car is capable of carrying three pucks. Sample processing, including plasma irradiation, Al single-atom deposition, and sample cleaning using a diode laser, was conducted on the top floor. Imaging and atom manipulation experiments were performed on the ground floor, where the STEM room and its control unit room are located. (Adapted from Ref. [23] with permission.)

2.5.1 Microwave Ar^+ plasma source for vacancy formation

When free electrons are subjected to a magnetic field \vec{B} , they rotate due to the Lorentz force with a natural frequency given by the Larmor frequency

$$f = \frac{eB}{2\pi m_e}. \quad (2.6)$$

Electron cyclotron resonance (ECR) microwave plasma can be produced by coupling these electrons to a microwave radiation with a frequency matches their natural frequency of

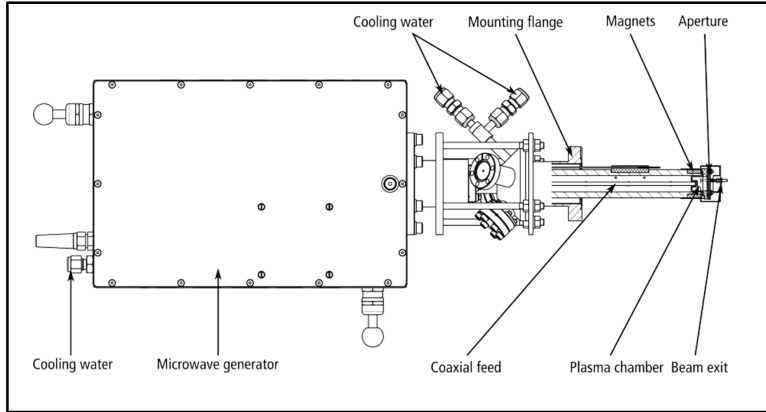


Figure 2.4: Schematic of the microwave ECR plasma source. Microwaves with 2.45 GHz are generated by the microwave magnetron and guided to the plasma chamber through a coaxial feed. The magnetic field causing the ECR phenomenon is generated by a magnetic quadrupole. The energetic electrons then ionize the gas in the plasma chamber and a large ion current is produced. During the process a lot of heat is generated, therefore two water cooling circuits are integrated into the system. (Adapted from Ref. [62] with permission.)

rotation in the magnetic field. This will heat the electrons by resonance absorption of the microwave energy. The heated electrons collide subsequently with the atomic gas and ionize them producing a large ion current [63]. The ion current is usually in the order of μA and is used for various applications such as low-energy ion implantation and defect engineering in 2D materials.

Engineering defects in graphene using low-energy argon ion Ar^+ irradiation was reported in several studies [64, 65]. In this study we have used an electron cyclotron resonance microwave plasma source SPECS MPS-ECR for generating the Ar^+ ions. The microwaves are produced using a magnetron with a frequency of 4.5 GHz, which is then guided to the chamber through a coaxial feedthrough as shown in Figure 2.4. A magnetic field of about 87 mT is generated using a quadrupole magnet [66]. Using Equation 2.6 gives electrons rotating with the same frequency as the microwave frequency. The ion current can be measured using a Faraday cup for evaluating the plasma source performance. In our experiment before using plasma irradiation, first we cleaned the sample using the diode laser with a power of 1.6 W for 40 minutes. Then after that we ran the plasma source for one hour for degassing and stabilizing the source. The argon plasma glow has a purple color and can be seen through a viewport at the top of the chamber via a small mirror installed at the bottom of the chamber for this purpose. We used a magnetron current at 16 mA and the pressure in the plasma chamber was 5×10^{-6} mBar. The sample was then inserted for 2 minutes in a perpendicular orientation with respect to the plasma source current.

2.5.2 Thermal evaporation of Al impurities onto graphene

Physical vapor deposition refers to the process of transporting and depositing atoms and molecules of a vaporized material onto a substrate, which is typically utilized for surface engineering and thin film processing [67]. While several PVD techniques exist, such as sputtering and pulsed laser deposition [68], we will focus in this thesis on the thermal evaporation PVD process, as it was the method used for depositing Al impurities. In this method, the material is heated to a high temperature to produce a significant vapor pressure causing atoms to leave the surface [69]. The atoms then travel in a vacuum system to the substrate they are meant to be deposited on. A good vacuum condition is essential during the PVD process to lengthen the mean free path for collision of the atoms leaving the surface and to control and limit the gaseous contamination that may affect the quality of the deposition. Moreover, at constant temperature the flux of the vaporized material towards the target substrate increases with increasing pressure differential [67].

The deposition rate depends on the vaporization rate, which can be increased by heating the vaporized material to higher temperature leading to increase in the vapor pressure. The vapor pressure in pascals of metallic elements can be written as a function of temperature and is given by [70]

$$\log p = 5.006 + A + \frac{B}{T} + C \log T + \frac{D}{T^3} = \varphi(T). \quad (2.7)$$

This equation applies for both the solid and liquid phases of metals. The coefficients A , B , C , D vary for different metals and also for different phases of the same metal. The vapor pressure in mbar is then

$$p(\text{mbar}) = 0.01p(\text{pa}) = 10^{\varphi(t)-2} \quad (2.8)$$

The free surface vaporization rate (flux) of the metal can be expressed by the Hertz–Knudsen vaporization equation [67]

$$\frac{dN}{dt} = C \frac{p^* - p}{\sqrt{2\pi m k_B T}}, \quad (2.9)$$

where C is a constant, p^* is the metal vapor pressure at temperature T , p is the pressure above the surface of the metal (in the deposition chamber), m is the atomic mass of the vaporized metal and k_B is Boltzmann's constant. The maximum evaporation rate can be obtained when $C=1$ and $p=0$, which can be achieved under very good vacuum conditions and negligible surface contamination.

For the thermal evaporation of Al impurities onto the graphene sample, we heated an Aldrich aluminium -evaporation slug inside a crucible with 99.999 % trace metals basis using a Knudsen cell. The base pressure inside the deposition chamber when we started heating was 6.1×10^{-9} mbar at $T = 26^\circ\text{C}$. The target temperature was set to 955°C with a ramping rate of $20^\circ\text{C}/\text{min}$. When the target temperature was reached, we waited 10 minutes for the temperature to stabilize and then inserted the sample in the deposition

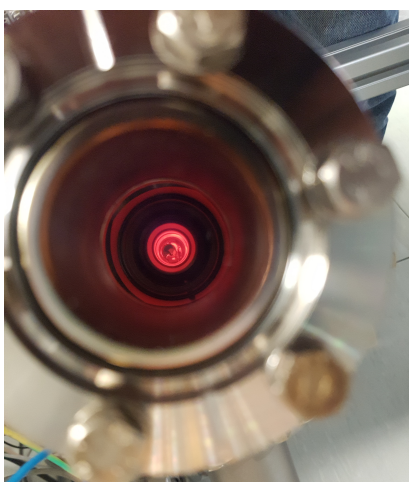


Figure 2.5: Image showing the Al slug when it started to melt inside the crucible during the thermal evaporation process.

chamber such that it faced the evaporation flux perpendicularly. The pressure when we inserted the sample was 3.7×10^{-8} mbar. During the process the gate valve to the chamber where the plasma irradiation is done was opened to pump out the surface absorbents and other gaseous contaminations that arise due to heating during the evaporation process. Figure 2.5 shows the Al slug inside the crucible during the process at slightly above its melting temperature of 660°C .

2.6 Automated single-atom manipulation

The controlled manipulation of single-atom Si impurities embedded in graphene was demonstrated for the first time by our group in 2017 using the Nion UltraSTEM 100 that was also used during this project [71]. However, the controllability was limited due to the lack of feedback. This was improved one year later by attaching a Keithley 2000 multimeter to the MAADF detector achieving a precise manipulation of a Si atom. It was able to perform 34 controlled jumps under the electron beam without any undesirable dynamics [72]. Yet, the electron beam was parked manually on each consecutive neighboring C atom, which is laborious and impractical, thus automating the manipulation is necessary for practical use. To address this issue, Andreas Postl in cooperation with other members in the group created the Nion Swift "Atom Manipulator" plugin [73] to automatically direct the process of manipulating single-atom impurities and rearrange them in a specific pattern set by the user. During this project, I was using the plugin for rearranging Si and Al impurities in graphene. For brevity, I will describe in this section only the basic functionalities of the plugin (a detailed description can be found in Ref. [23]) and the procedure of acquiring data during the experimental measurements.

2.6.1 Nion Swift Atom Manipulator plugin

The Atom Manipulator plugin is an open-source software designed to minimize the need for user input. The plugin has a graphical user interface that is embedded in Nion Swift, and it contains different modules that can perform various tasks. The main tasks of the plugin are [23]:

- **Structure recognition:** The structure recognition module performs a spatial calibration of the image and then uses a fully convolutional neural network (FCNNs) to recognize the atomic structure and identify foreign atoms. The spatial calibration can be operated in two modes either in real space using the NN or in reciprocal space using Fourier scale calibration. In our experiment, the real space mode was mainly used (occasionally when this mode failed I was switching to Fourier space).
- **Bond detection:** This task is implemented within the Structural pathfinding module, which assigns a bond between two carbon atoms if the inter-atomic distance between them is less than a specific threshold set by the user (in our experiment the max bond length was set to 2.2 Å). It also defines a maximum for the number of bonds a carbon atom can have, which is set to 4.
- **Structural pathfinding:** In this task the minimum total path length between N impurities and M user-defined target sites is calculated using the Hungarian algorithm [74, 75]. This algorithm considers the overall task and determines the path that results in the lowest performance cost. The structure pathfinding module is implemented in such a way that the path between an impurity atom and its user-defined target site avoids passing through any other impurity, its nearest neighbours, as well as the second-nearest carbon neighbours of any impurity as illustrated in Figure 2.6.
- **Detection of successful jumps and of drift:** This is accomplished using the Keithley multimeter, which is connected to the MAADF detector. The multimeter reads the voltage changes and interprets them as a direct exchange event (jump) between the impurity and the PKA or as a sample drift according to the user-defined threshold in each case. The feedback from the MAADF detector is communicated through the TractorBeam module in the plugin. During our automated manipulation experiments, the Tractor time was set to 15 s, which means the electron beam was parked on the PKA for 15 seconds. This is relatively a short Tractor time, but it was chosen considering the drift of the sample. Then the TractorBeam provides a feedback if there was a jump or a drift during this 15 s. After that the electron beam was repositioned according to the path and the process was then repeated again. The threshold for detecting jumps was set to 15% during our all atom manipulation experiments, but the drift threshold was changed between two values: 4% for small drift and 6% for notable drift, depending on whether a large sample drift was present or not.

All the previous tasks' related commands are translated via the Nion Swift API to the hardware control unit of the STEM.

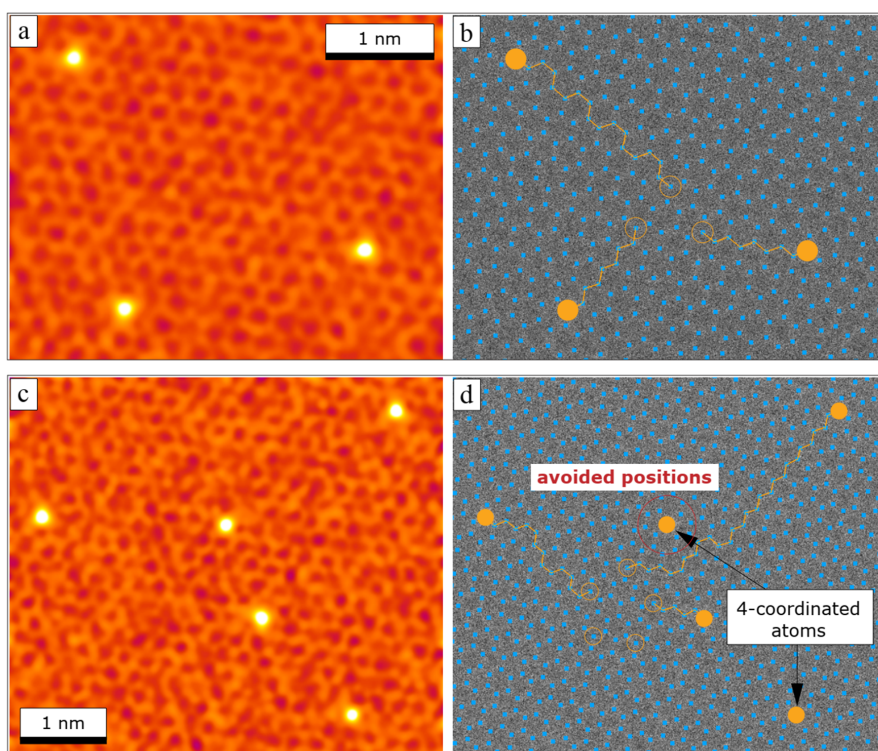


Figure 2.6: Images illustrating the functionality of the structural pathfinding model integrated in the plugin. Left: Colored Gaussian-filtered images of graphene with single-atom impurities embedded. (b, d) The corresponding raw images with overlays for recognizing the lattice structure. The foreign atoms are indicated with solid filled circles with orange color. The target sites are highlighted with non-filled orange circles and the calculated paths between the impurities and their user-defined target sites are marked with solid orange lines. (Adapted from Ref. [23] with permission.)

2.6.2 Experimental procedure and data acquisition

The experimental session begins with searching for a suitable hole in the support film that meets specific criteria. Firstly, the hole must be free of any mobile contamination. Secondly, the chosen hole should contain small, clean patches of graphene that form the regions of interest (ROI) of the user. Ideally the ROI should have many 3-fold single-atom impurities incorporated into them, which should be distant from each other. An area of approximately 20 nm^2 or larger should be sought after. Finally, the selected area for the manipulation experiment should not be excessively corrugated or defective.

Successful automated single-atom manipulation requires a reasonable compromise between image time and the contrast of the image. The contrast in STEM images is represented

2 Methods

by the signal to noise ratio (SNR):

$$\text{SNR} = \frac{S_s}{S_n}, \quad (2.10)$$

where S_s is the average intensity of the signal, which comes from the atoms in the image, and S_n is the intensity of the background, which is here simply the vacuum. While a minimum level of contrast is necessary for the user to recognize atomic structures visually, the neural network in the structure recognition module, which is integrated in the plugin, can still recognize atomic structures to a certain degree even with a poor contrast [23]. In addition, the Nion Swift software has many filters for improving the contrast of the images and decreasing the noise present in them (a Gaussian filter was always used for this purpose). The SNR in STEM can be increased by increasing the current beam, by using a better detector, or by increasing the dwell time (the time the probe spends on one pixel) [76]. During our experiments we only increased the extraction voltage slightly when needed. Increasing the dwell time during the manipulation comes with the drawback of having greater sample drift in the recorded frame and reducing the time resolution, thus this was avoided as well.

The time needed for recording one frame is given by the number of pixels in the frame $N_x \times N_y$ multiplied by the dwell time t_p . Thus the dwell time and the number of pixels in the frame were chosen such that good time resolution is obtained, but at the same time retaining a reasonable SNR such that the contrast of the image was still sufficient for structure recognition by the neural network. A frame of 512×512 pixels was used most at the time. Dwell times of 4, 6 or 8 μs were used depending on the microscope conditions and the field of view (FOV) size.

When choosing the FOV, it was noticed that using a large FOV (larger than $4 \times 4 \text{ nm}^2$) can lead to more frequent structure recognition failure and often containing more contamination in the frame depending on the size of the clean graphene patch, while using arbitrary small FOV comes with the drawback that the impurities we are manipulating or their target sites come close to the frame edge after only few frames due to the stage or sample drift and are not being recognized by the neural network anymore. For these reasons, the FOV used during our experiment was $2 \times 2 \text{ nm}^2$ in most cases, though sometimes a FOV of $4 \times 4 \text{ nm}^2$ was used when the microscope was in a good condition and the ROI was flat with no defects or contamination, or when we wanted to include many impurities in the manipulation process with the aim of drawing a simple pattern.

When using the graphene sample with Al impurities, the single-atom dopants were identified using EELS. For this a dispersion of 0.16 eV/pixel was used. Acquiring a signal coming from a single atom is challenging due to both the low SNR and the presence of sample drift. For mitigating the drift, we sometimes positioned the electron beam slightly ahead of the target impurity to compensate for it. In addition, many EEL spectra were recorded for each impurity and the best were selected and used in this thesis. While a longer acquisition time usually results in improving the SNR, the sample drift will result

2.6 Automated single-atom manipulation

in collecting signal from the target atom for only a portion of the time when the impurity is still under the electron beam, and the rest of the signal will arise from the background when the impurity has shifted away as a result of the drift. Thus the acquisition time cannot be chosen very long, not more than a couple of seconds.

After the impurity atom is identified by EELS, the automated manipulation can be started by creating a new data item using the plugin and then simply starting the process using the option "Start automated manipulation". This will launch the structure recognition module, which then identifies the impurity as a foreign atom. The target site where the impurity is desired to be moved can be set by the user. After that the Pathfinding module will calculate the optimal path to bring the impurity to the target site as described in Section 2.6.1. Then the plugin will command the microscope to park the electron probe on the target that is defined from the calculated path and start iteratively manipulating the impurity atom.

3 Results and discussion

In this chapter I will present the results I obtained during the experimental work and discuss them in detail. First, I will present the results of each step of the sample preparation process, including sample cleaning, plasma irradiation, and Al deposition. Second, I will present and discuss the successful automated single-atom manipulation (by successful, I mean a single jump of the atom in the desired direction and not necessary that the manipulated atom reaches its defined target site at the end of the process), as well as some interesting cases and events observed during the manipulation of both Si and Al impurities. Finally, I will address the challenges and difficulties encountered during this work.

3.1 Laser cleaning effect

After loading the graphene sample into the vacuum system and observing it with the STEM, it looked quite dirty and almost fully covered with contamination as shown in Figure 3.1.a. Any large patch of clean graphene was not found, but small clean areas up to 40 nm^2 in size were accessible. One of the good features of the thick silicon nitride grid is its robustness and its ability to withstand high temperature. This facilitated the cleaning of the sample and allowed us to use laser annealing as mentioned before. Figure 3.1 shows the cleaning effect by comparing between two different regions before and after using the laser. Clean graphene area of about 10^4 nm^2 in size were readily found as the patch in Figure 3.1.b.

The power of the diode laser used for cleaning was chosen carefully and reasonably small to avoid any damage to the sample. There were only three freestanding areas (windows) cleaned and in two of them most of the fixed contamination was removed after cleaning, but the thicker contamination was still present (Figure 3.1.b). This remaining contamination can form a wall-like barrier that helps block mobile hydrocarbon contamination from diffusing over the surface of the graphene sample. In the third cleaned window most of the thicker contamination was removed as well, but we did not observe any mobile contamination.

Using a radiative cleaning method can lead severe to thermal drift in the sample [51], but luckily this was not observed at the power we used. The temperature the sample surface reaches during laser cleaning can be estimated after reaching a thermal equilibrium state using Stefan–Boltzmann law. Graphene is a highly conductive material and this should be taken into consideration when trying to estimate the deposited heat [51].

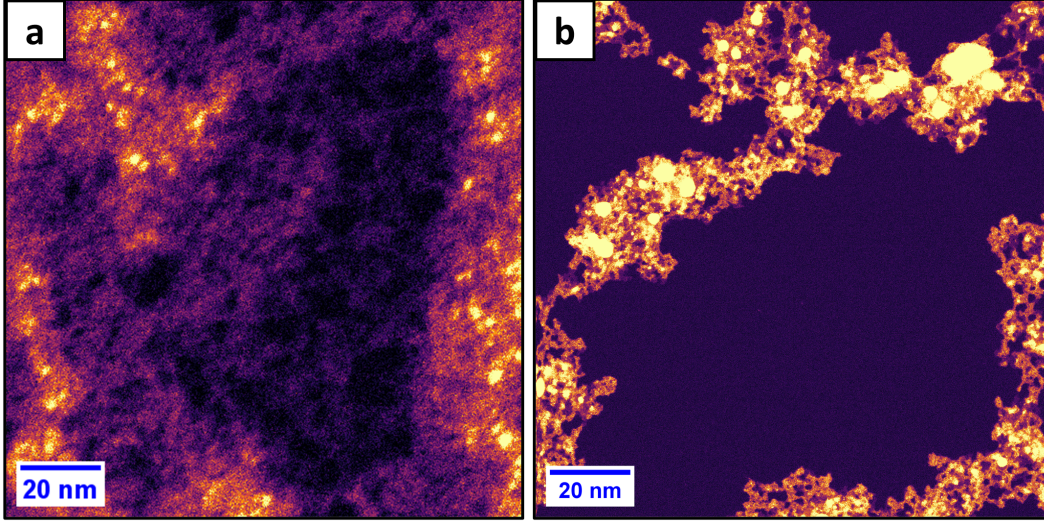


Figure 3.1: STEM images showing the cleaning effect of the laser on the graphene sample. (a) and (b) show colored MAADF images (FOV = 128 nm) of graphene lattice before and after cleaning the sample. In (a) the surface was covered with contamination and only small areas of clean lattice were found, while after cleaning a whole patch of clean graphene lattice (dark contrast) with an area of about 10000 nm^2 was found. However, the vacuum laser annealing could not remove the thicker contamination (bright contrast) shown in (b).

3.2 Vacancies and nanopores after plasma irradiation

Low-energy ion irradiation using noble gas ions has been shown to be an efficient method for creating single and double vacancies in the graphene lattice [58], which made it the obvious choice for our defect engineering experiment for later incorporation of Al single atoms into these defects. Having SV and DV defects was predicted since the energy of the Ar^+ ion beam was higher than the minimum kinetic energy required for displacing one carbon atom, which can be calculated from Equation 2.3. In the case of Ar ions, the minimum energy was calculated by using a displacement threshold energy of $E_d = 22.2 \pm 0.2 \text{ eV}$ giving $E_{\min} = 32.74 \pm 0.15 \text{ eV}$ [77]. At a pressure of $5 \times 10^{-6} \text{ mbar}$, the majority of the Ar^+ ions have energies of about 102 eV and 148 eV. These two values were obtained from ion current measurements using the Faraday cup done by colleagues in our research group. This can be inferred from the increase in the negative current at these two energies, where positive ions with these energies are decelerated and cannot reach the Faraday cup leading to the abrupt increase in the measured negative current as shown in Figure 3.2.

The ion beam diameter at the source is 1.3 cm [78] and the distance between the source and the sample in our experimental set up was 4.7 cm. Using this, we can calculate the beam diameter (spot size) at the sample using the relation [62] $d_{\text{sample}} = d_{\text{source}} + 2 \times 4.7 \times \tan(15)$, which gives a spot area at the sample of $A = \pi r^2 = 11.5 \text{ cm}^2$. The calculated ion dose is

3 Results and discussion

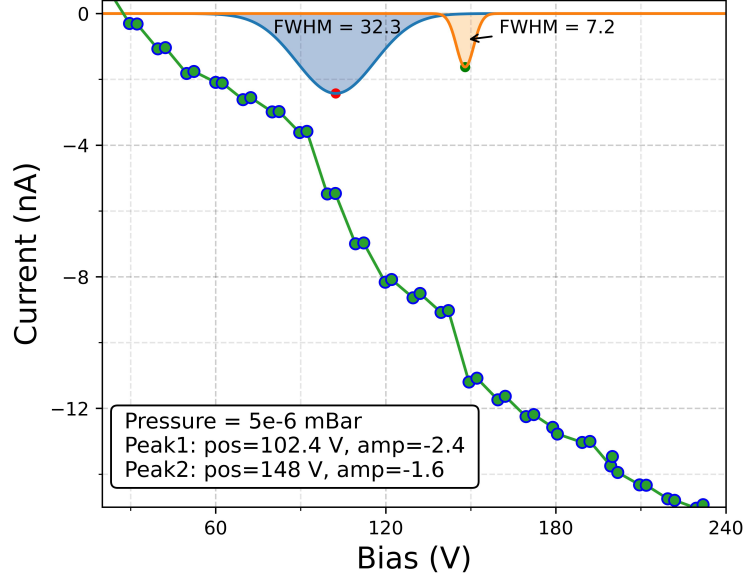


Figure 3.2: Measurement of the Ar^+ ion beam current using a Faraday cup (represented by the blue dots) as a function of the positive bias at a pressure of about 5×10^{-6} mbar. The negative current measured increases drastically at the two bias values of 102 and 148 V, due to the decrease of the ion beam current at these low values. This suggests that the majority of the ions have one of these energies. Thus, Gaussian curves were used to represent the ion beam, in which their peaks are positioned at these two energies. Fitting of the data was done by integrating over the two Gaussian curves and a linear function representing the increase in the negative current. (The parameters of the two Gaussian curves were obtained from fitting the data and provided from colleagues Manuel Längle and Vinzent Hana. The data of the current plot and its fitting were extracted using the WebPlotDigitizer app and used in this figure, while the two Gaussian curves were plotted using the parameters provided.)

$n = \frac{It}{eA} = 0.4 \times 10^{13}$ ions/cm², where t is the time the sample was inserted in the plasma chamber and I is the ion beam current calculated by integrating over the two Gaussian curves.

After the Ar^+ bombardment, the lattice looked heavily damaged in two of the three windows that underwent laser cleaning. The third window was relatively unaffected by the irradiation and remained structurally intact. In the two windows that looked affected by the plasma irradiation, a wide variety of defects were observed ranging from single vacancies to larger defect complexes and nanopores as depicted in Figure 3.3. The presence of defect complexes and nanopores is not expected to result from Ar^+ ions

3.2 Vacancies and nanopores after plasma irradiation

bombardment and suggests that additional factors such as chemical etching may have led to their formation.

The acquired images after performing the plasma irradiation were analyzed to estimate the size and area of the large defects. This was done using a Python script that performed image segmentation using the thresholding method. In this method, the background (defects) was assigned as an object. Subsequently, the smaller defects were filtered out, and the size (Ferret's diameter) of the large defects (contours) as well as their areas were calculated and saved.

The diameter of the large defects in the images we had ranged from 0.4 nm to 1.4 nm with an average of about 0.7 nm and the average area was 0.2 nm^2 . This suggests the presence of oxygen in the plasma chamber during the irradiation process, as the resulting pores resemble those obtained via oxygen plasma etching, which is used for tailoring pores in graphene-based materials [79].

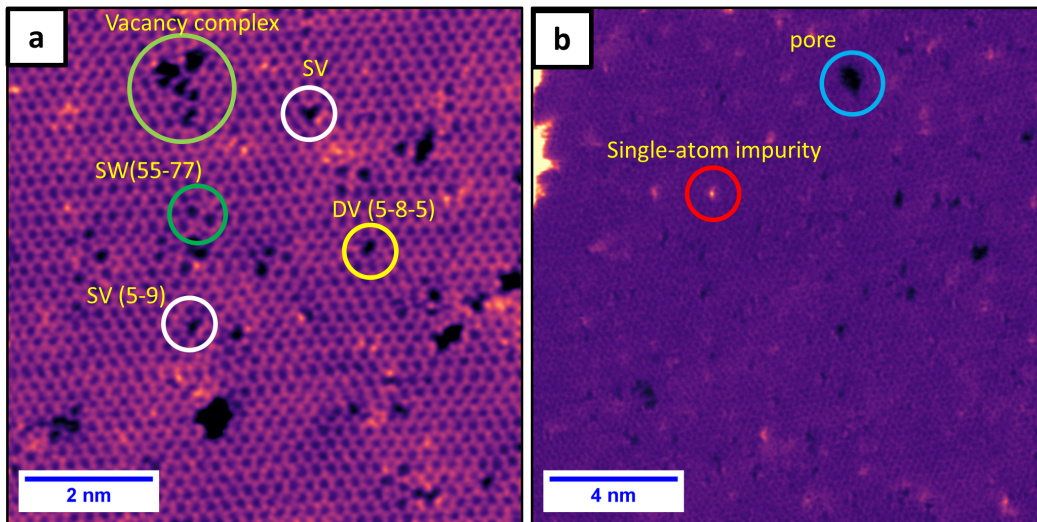


Figure 3.3: Defective graphene lattice after being subjected to Ar^+ plasma irradiation. (a) Colored MAADF image filtered using a Gaussian blur ($\text{FOV} = 8 \text{ nm}$) shows a heavily defective area of graphene lattice with many different types of defects recognized as $\text{SV}(5-9)$, $\text{SW}(55-77)$ and $\text{DV}(5-8-5)$. The Al impurities incorporated later in the lattice take a 3-fold configuration when being incorporated in SVs, while having a 4-fold configuration when filling DVs. (b) Gaussian-filtered MAADF image ($\text{FOV} = 16 \text{ nm}$) shows a defective graphene lattice structure with a nanopore defects, with the indicated one (in blue circle) measured to have a Ferret's diameter of about 1.1 nm and an area of about 0.55 nm^2 .

3 Results and discussion

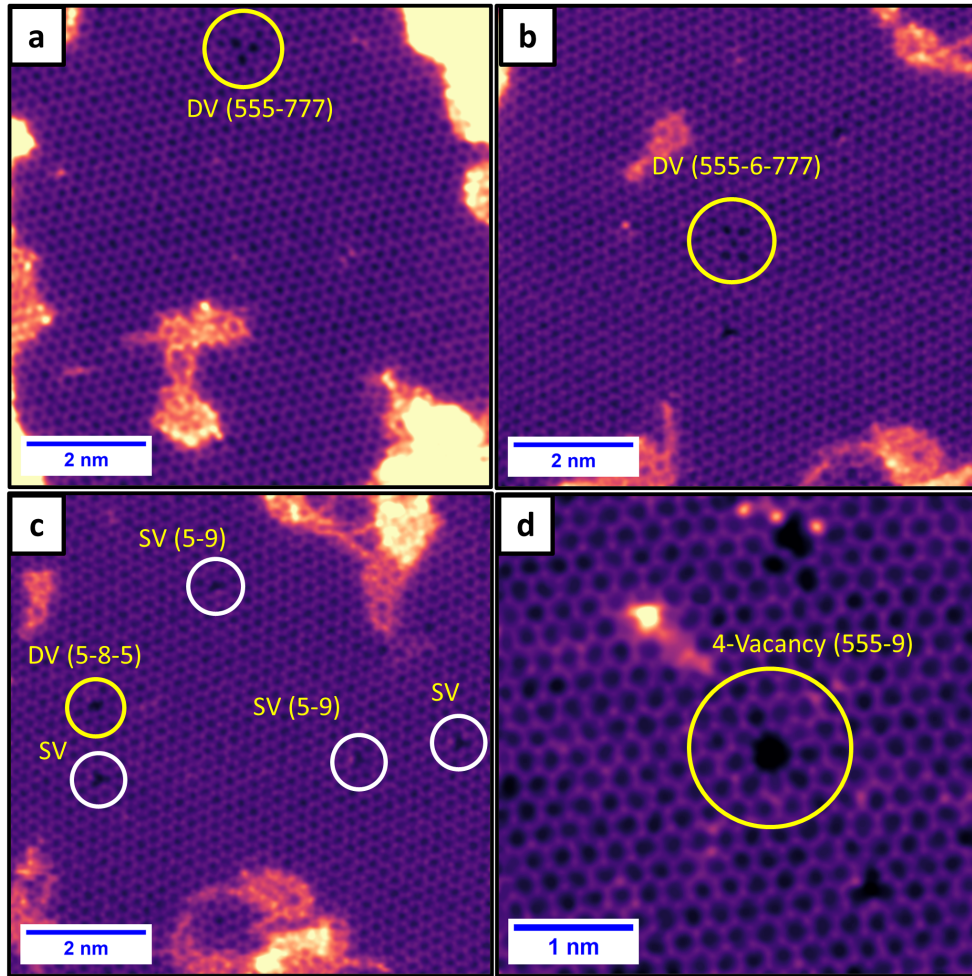


Figure 3.4: Gaussian-filtered MAADF images of graphene after Ar^+ plasma irradiation and laser annealing that show a variety of defect types in the lattice. (a) DV(555-777) defect configuration that results usually from a bond rotation of the DV(5-8-5) [16]. (b) DV(555-6-777) defect that result from a further bond rotation from the DV(555-777). (c) A nice graphene area with many SVs, which is optimal for incorporating 3-fold single-atom Al impurities into them. (d) An interesting defect configuration (555-9) that consists of four vacancies.

A highly defective graphene lattice is not optimal for single-atom manipulation, therefore the sample was treated with the laser to heal the defects using a laser power of 0.72 W for 10 minutes. Vacuum annealing at high temperature has been suggested as an efficient method for defect healing [80], where hydrocarbon contamination and carbon adatoms are provided with sufficient energy to migrate and diffuse across the graphene lattice and recombine with the defective sites [81]. The first laser treatment appeared to provide a

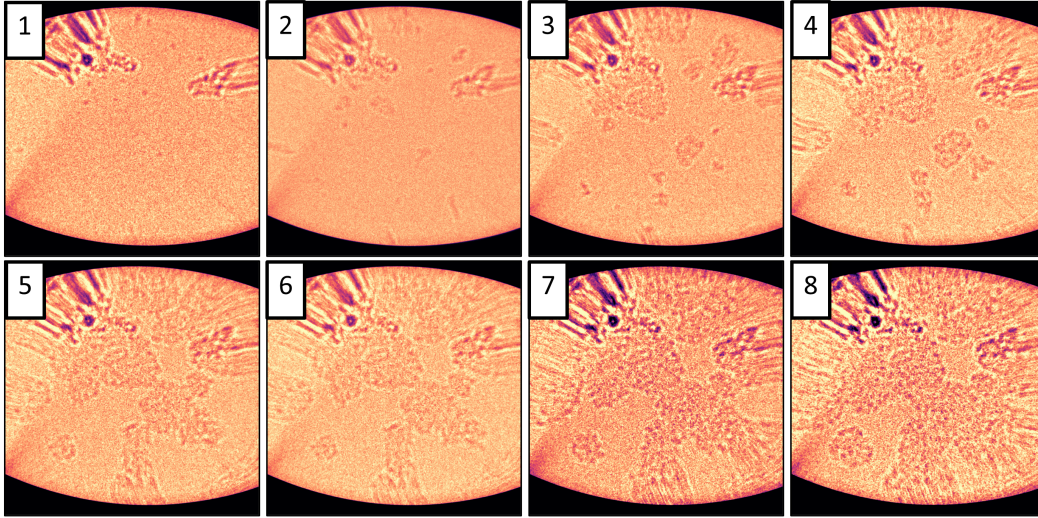


Figure 3.5: Sequential STEM bright-field snapshots that show the accumulation and growth of pinned mobile contamination under the electron beam. The time of the whole image series was 27 s, where in the last snapshot almost the whole area was covered.

slight improvement. Consequently, the process was repeated with a higher laser power of 1.2 W for 20 minutes, resulting in a less defective graphene lattice as observed using the STEM. However, as a result of the plasma irradiation and subsequent laser treatment, numerous structural defects were identified, as shown in Figure 3.4. The observed known defects include single vacancies (SV), SV(9-5), double vacancies (DV) such as DV(5-8-5), DV(555-777), DV(555-6-777) and SW(55-77) in addition to an intriguing 4-vacancy defect with the configuration (555-9).

One of the major obstacles that hinders experimental measurements is the presence of diffusing mobile contamination on the graphene surface. This is because they become pinned by the electron beam to the surface and thus accumulate until eventually covering the ROI as shown in Figure 3.5. To mitigate this issue, we tried two different methods.

The first method is to use the column laser integrated into the STEM by illuminating the ROI for about 5 to 10 s with a laser power up to 40 mW (laser pulses were not useful in this respect). This helped sometimes for a short time (15 to 30 minutes inconsistently) and then the contamination starts to diffuse again over the surface.

The second method employed the so-called beam showering, whereby the entire area was exposed to the electron beam for approximately 15 to 30 minutes. While this method occasionally provided some help, similar to the case of the laser illumination, mobile contamination starts to reappear again after a short period of time. The mechanism

3 Results and discussion

behind the removing of mobile contamination in both methods is not clearly understood, and many times neither method was effective in removing them. For this reason, during our experiment, whenever we encountered mobile contamination, we would switch to a different region and investigate another area.

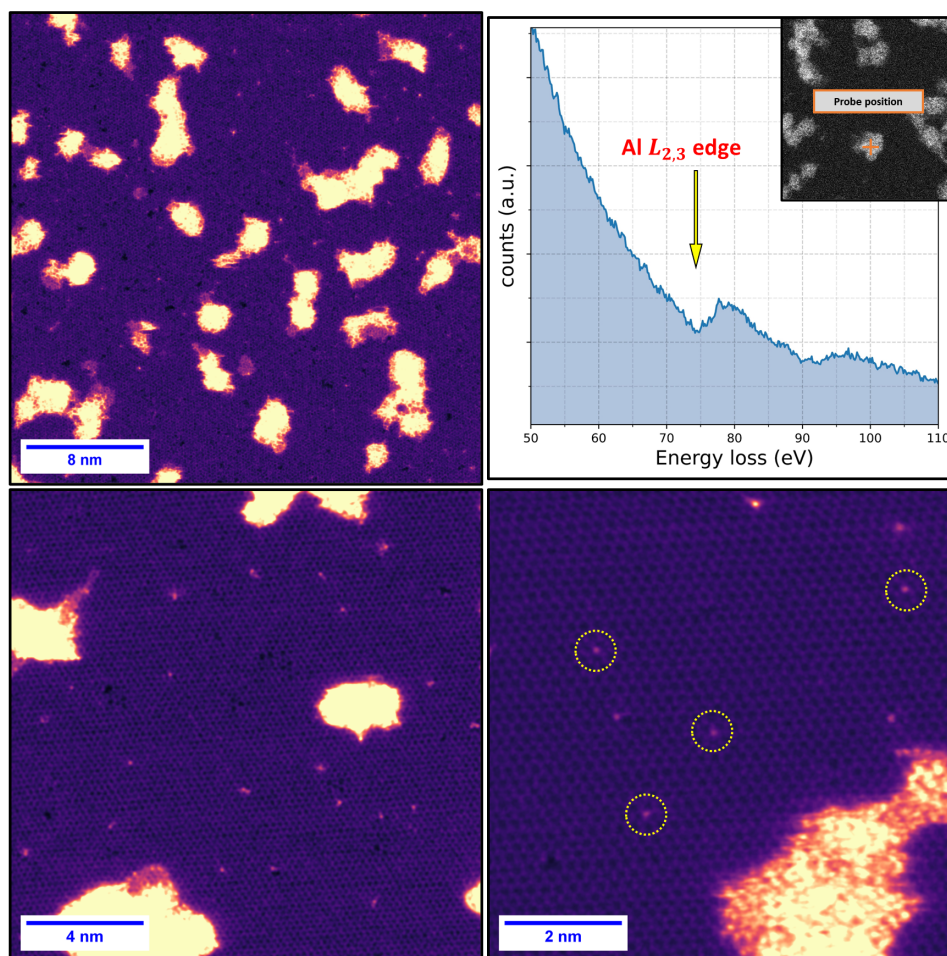


Figure 3.6: MAADF images of graphene after depositing Al. (a) Graphene lattice (dark contrast) covered with nanocluster islands of Al (bright contrast). (b) EELS of the Al $L_{2,3}$ edge at about 73 eV of one of the clusters that confirms successful deposition. (c) Gaussian-filtered image (FOV = 16 nm) that shows the high heteroatom coverage, however not all the single-atom impurities are Al but a significant portion are indeed Si. (d) Closer view of the graphene lattice (FOV = 8 nm) that shows many 3-fold single-atom impurities (marked with yellow dashed circles) incorporated into the graphene lattice.

3.3 Incorporation of Al into the graphene lattice

After forming vacant sites for single-atom impurities in the graphene lattice using plasma irradiation and subsequent laser annealing, Al impurities were successfully deposited on the sample by thermally evaporating an Al slug as mentioned in the previous section. The sample was covered with Al nanoclusters as shown in Figure 3.6.a. This was confirmed by EELS and verified from the presence of the Al $L_{2,3}$ core-loss edge at about 73 eV as shown in Figure 3.6.b. Single heteroatom coverage after the deposition process was relatively high in one of the three windows that were previously successfully cleaned with the laser. One window had mobile contamination making it not suitable even for imaging. The other window that was not affected by the plasma treatment had a very low density of substitutional impurities, which is due to the absence of defects that can hosts the deposited Al atoms or migrating on the graphene surface.

The density of the deposited Al atoms on the graphene sample can be calculated theoretically by obtaining the flux rate of the evaporated material using Equation 2.9. For that we need to calculate the vapor pressure of the melted Al slug at 955°C, which can be obtained from Equation 2.7 knowing that the coefficients for the case of melted Al are [70] $A = 5.911$, $B = -16211$, $C = 0$ and $D = 0$, resulting in

$$\varphi(T) = 10.917 - \frac{16211}{T}, \quad (3.1)$$

which gives a vapor pressure of 5.26×10^{-5} mbar when substituted in Equation 2.8. The residual pressure in the deposition chamber when we inserted the sample can be neglected compared with the Al vapor pressure. Based on that the maximum flux rate during the Al deposition process was about $762 \times 10^{15} \text{ atoms s}^{-1} \text{ m}^{-2}$. The sample was inserted only for 5 s in the deposition chamber, which yields a density of 3.8 atom nm^{-2} . By analysing the images we obtained after the deposition we got a heteroatom density in the graphene lattice of about $0.14 \text{ atom nm}^{-2}$. This difference can be explained by the nucleation of most of the evaporated Al impurities Al nanoclusters.

3.3.1 Distinguishing between Al and Si atoms

Having many Si impurities in the graphene sample we deposited Al onto required us to verify that what we are manipulating is indeed Al and not Si. For this we acquired EEL spectra of the dopants. Since the signal is being collected from a single atom, the features indicating the chemical nature of the dopant in the spectrum are not very pronounced. Figure 3.7 shows a comparison between high-signal EEL spectra of Al and Si impurities. While the Al $L_{2,3}$ core energy-loss edge onset is at about 73 eV, the Si $L_{2,3}$ core-loss edge onset is at about 100 eV. It is worth noting that both the Al and Si atoms were at defective lattice sites. For further verification, the intensity of the dopant under investigation was compared with the other dopants present in the image by integration over a circular area of the same size around them using ImageJ. Based on the Z -contrast of the MAADF detector in our STEM instrument, the ratio between the measured intensities of Al and Si

3 Results and discussion

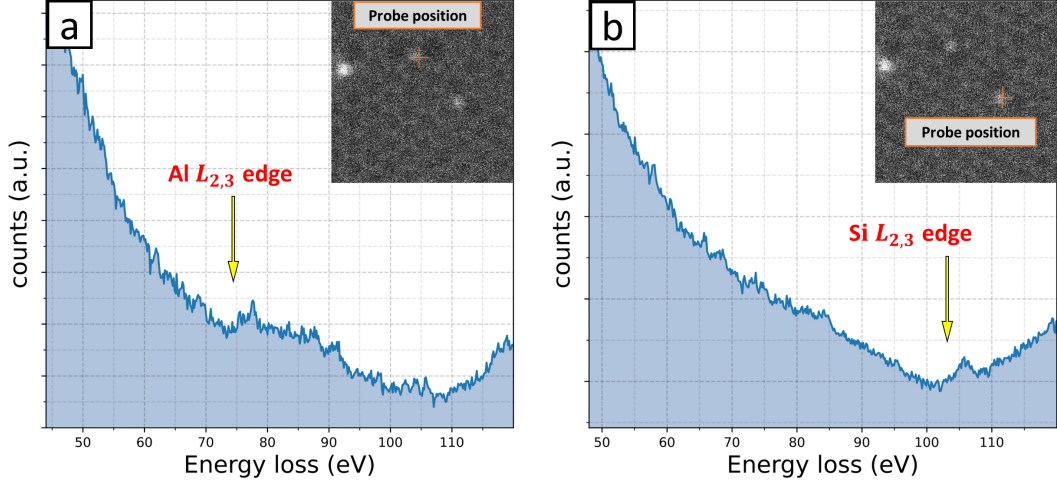


Figure 3.7: EEL core-loss edge spectra of Al and Si for comparison. (a) EEL spectrum of the dopant shown in the inset MAADF image, which shows a feature corresponds to the Al $L_{2,3}$ core-loss edge with an onset at about 73 eV. (b) EEL spectrum of the impurity shown in the inset MAADF image showing a feature corresponds to the Si $L_{2,3}$ core-loss edge at about 100 eV. The rising background around 105 eV was due to a reflection in our spectrometer.

atoms should be about $\frac{I_{\text{Al}}}{I_{\text{Si}}} = 0.89$. The intensity ratio of the Al and Si impurities shown in Figure 3.7 is about 0.91, which is in a reasonable agreement with the theoretical value. Thus, combining both the EELS measurement and the measured Z -contrast ratios using the integrated intensities should be sufficient evidence of the identities of the impurity atoms.

3.4 Automated single-atom manipulation

This project was initiated with the objective of conducting controlled automated manipulation of both Al and Si single-atom dopants in graphene using the focused electron probe of STEM with the primary aim to explore the feasibility and limitations of this process. The ultimate goal was to achieve the precise arrangement of at least three single atoms to form a pattern. In this section I will discuss the various competing events during the automated-manipulation process to give more insight about its efficiency.

In the presented results, both Gaussian-filtered and raw images with overlays generated by the atom manipulator plugin will be provided. In addition to the overlays for recognizing the atomic structure, the detected foreign atoms, the defined target sites and the calculated path will be marked as well. A beam current of about 19.4 ± 0.6 pA at the accelerating voltage of 60 kV used during the experiments was obtained using beam current measurements done by colleagues in the group [82]. Based on that, a dose

3.4 Automated single-atom manipulation

Table 3.1: Summary of automated single-atom manipulation results for both Si and Al impurities. XCEX denotes a successful controlled manipulation event where the impurity jumps to the defined target site (X stands for the impurity, thus in the case of Si impurity, this will be SiCEX). XCKO represents knock-on damage of a neighboring carbon atom, transforming the impurity from a 3-fold to a 4-fold configuration. XRepC refers to the replacement of the impurity with a diffusing carbon atom. XKO stands for the ejection of the impurity, leaving behind a single vacancy. XDJ corresponds to a double-jump, where the impurity appears to move over two lattice sites. XUid refers to any unintended single jump of the impurity to a lattice site different from the defined one by the Pathfinding module.

	XCEX	XCKO	XRepC	XKO	XDJ	XUid
Si	67	4	3	0	10	14
Al	12	2	0	2	0	4

rate of $(1.20 \pm 0.04) \times 10^8 \text{ e}^- \text{ s}^{-1}$ was estimated. The probe shape is a combination of Gaussian curves with a FWHM of 1.1-1.4 Å [23], which means not all the electron dose is impinging on the targeted C atom. It was estimated that only 26% of the dose is hitting the target C atom for a Gaussian probe shape with FWHM of about 1.4 Å [72, 83]. Thus in our experiment and taking the drift into account, an estimation of only 20% of the dose impinging on the targeted C atom seems reasonable.

3.4.1 Efficiency of manipulation in the presence of competing processes

As explained in Section 1.6.1, single-atom manipulation of a dopant atom in graphene using STEM occurs due to targeting a C neighbor with the electron beam leading to a direct exchange process between the dopant and the targeted C atom. Nevertheless, many other competing undesired process and configurational changes in the structure can arise under the electron beam. Thus having a successful single-atom manipulation can be limited by these competing processes.

For consistency, I will be using the same acronyms and terminology as Dr. Andreas Postl in his PhD thesis for describing these processes. For both a bond inversion process and two Stone-Wales rotation events that lead to the equivalent result of positional exchange between the X dopant atom and the targeted C atom resulting in moving the impurity to the desired target site, the acronym XCEX will be used indicating a controlled direct exchange process between the C atom and the X dopant. Thus the cross section of a successful manipulation event can be described as σ_{XCEX} . Knock-on damage of a neighboring carbon atom, which causes the transformation of the impurity from 3-fold to 4-fold configuration, will be referred to as XCKO, and the cross section of this process σ_{XCKO} . The acronym XRepC represents the replacement of the impurity atom with a carbon

3 Results and discussion

atom. The cross section for this process is denoted σ_{XRepC} . During our experiments, this process was observed when manipulating Si atoms but not for Al atoms, as were observed to leave a single vacancy behind being knocked out of the graphene lattice by the electron beam. This process will be referred to as XKO, and its cross section is denoted as σ_{XKO} . This was never observed for Si impurities during our experiments. In addition to these processes, it was sometimes observed that the dopant jumped in a direction different from the defined one. These uncontrolled jumps can be classified as an undesired processes and will be denoted XUid (unintended jump of the X dopant), with a cross section referred to as σ_{XUid} . Finally, double jumps were frequently observed and since they occur in most cases not according to the defined path calculated by the Pathfinding module, they are considered as another undesired process and will be denoted XDJ with a cross section σ_{XDJ} .

Based on the above, the degree of controllability, which reflects the efficiency and success of automated manipulation can be described by the probability that parking the electron beam on the C neighbor of the dopant will result in a direct exchange process between them that move the impurity to the defined target site. Experimentally, this can be obtained from the ratio between the number of observed controlled successful manipulation event to the total number of observed various competing processes induced by the electron beam when a reasonably large set of experimental data are available.

$$\eta = \sum_{\alpha} \frac{\Omega N_{\text{XCEX},\alpha}}{\sum_{i=1}^n N_{i,\alpha}}, \quad (3.2)$$

where n is the total number of the competing processes under the electron beam during automated manipulation. Ω is the total number of automated single-atom manipulation experiments conducted and $N_{i,\alpha}$ gives us how many times the process i was observed during experiment α . For large Ω , this can approximate the ratio between the cross section of the direct exchange process to the sum of the cross sections of all competing processes during automated-manipulation, if the double jump process would lead to moving of the impurity according to the calculated path and thus considered as a desired outcome. The outcomes of our automated-manipulation experiments is summarized in Table 3.4.1. While we recorded 67 successful controlled manipulations of Si atoms, we managed only 12 times to successfully manipulate Al dopants. Based on the data we obtained and using Equation 3.2, the automated-manipulation efficiency for Si single-atoms was about 67% and about 60% for Al.

3.4.2 Six successful controlled jumps of a Si dopant

One of the first successful automated manipulations of a Si impurity was performed in August 2022 and includes 5 successive controlled jumps as shown in Figure 3.8: from frame 3 to 13 it followed the path calculated by the plugin approaching the user-defined target site. After performing the 5th jump, it committed an undesired double jump (frame 13 to 16). After this it did another controlled jump back to the original lattice site it was supposed to end at in frame 13. Then it performed another undesired jump and

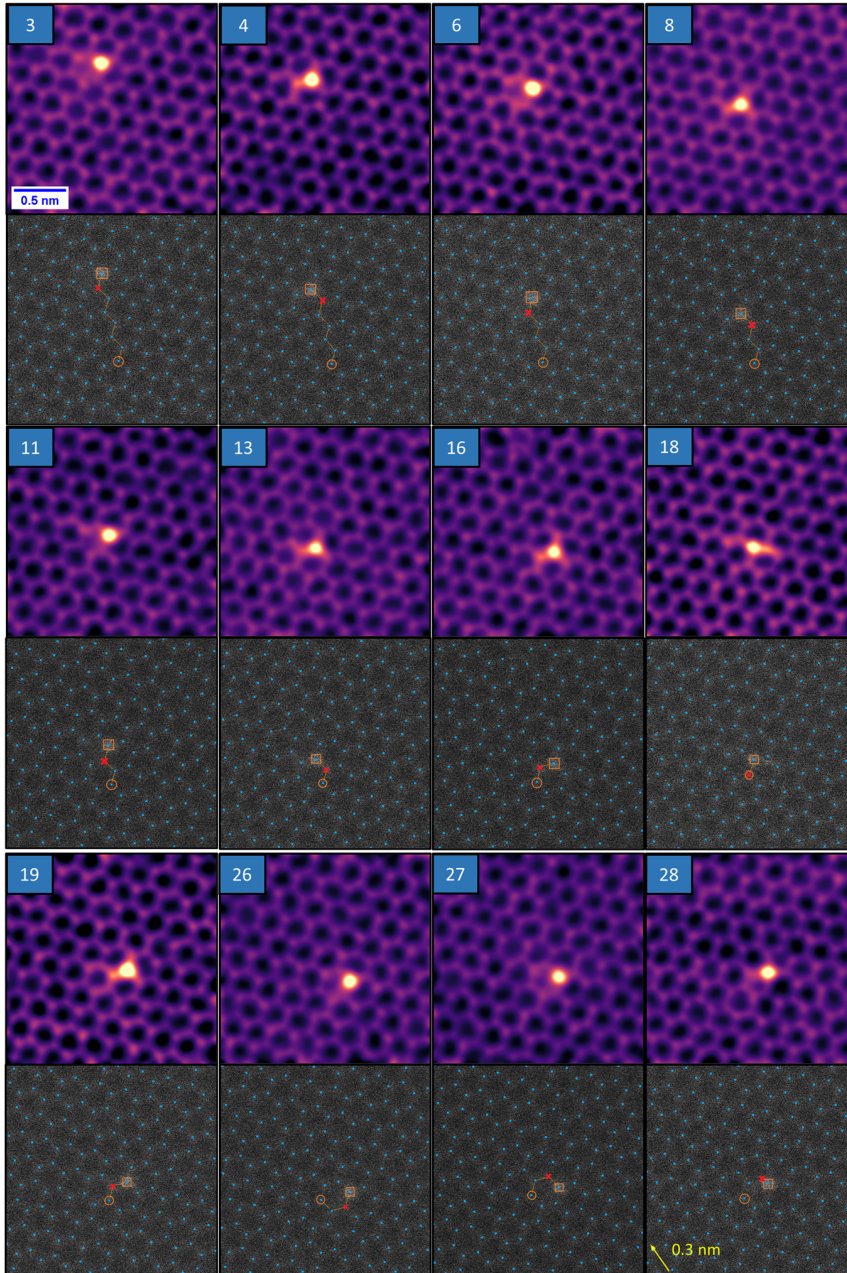


Figure 3.8: MAADF image sequence of the automated manipulation of a single Si atom (total of 28 frames, only ones that include new events are depicted and the frame number indicated). Colored Gaussian-filtered images on the top, and the plugin-generated raw images with overlays on the bottom. The impurity is marked with an orange square and the defined target site with an orange circle. The calculated path is shown as thin orange lines and the electron-beam position as a red cross. The Si performed six successful jumps, one double jump and one jump to a different lattice site than intended. At the end, the Si turned into 4-fold configuration after knock-on displacement of one of its C neighbors.

3 Results and discussion

moved back to the lattice site it was at before committing the double jump. Finally, one of its carbon neighbor atoms was knocked out and it transformed from 3-fold to 4-fold, which cannot be manipulated and the process therefore was terminated.

The drift during the manipulation process was modest at about 0.1 \AA per frame, as calculated using a reference lattice site in the first frame and tracking its movement to the last frame and measuring the distance it passed during the process. Although that the drift happens in a random direction but there was an overall direction, this was consistent across the frames.

The double jump can be thought of here as one controlled jump to the site at which the electron beam is positioned (indicated with the red x) followed by an unintended jump. But since we are blind to events occurring while the electron beam is parked and during the following frame scan time, and since the second jump (assuming the double jump is indeed two separate jumps) was not to the next lattice site defined and calculated using the Structural Pathfinding module, the double jump is not treated as two successful controlled jumps. Instead it is considered as undesired dynamics during automated manipulation.

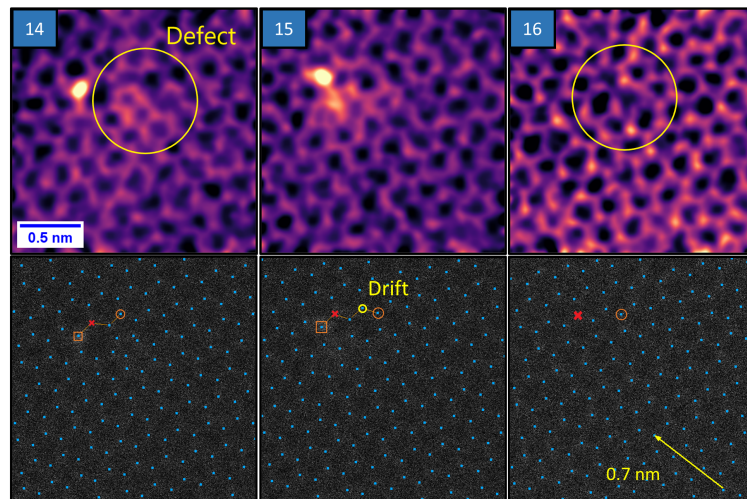


Figure 3.9: MAADF image series during a manipulation trial of a single Si atom in the presence of large drift. The Si atom was not manipulatable and got lost from the lattice being replaced by a carbon atom. The small yellow circle shows changing the defined target site due to drift. The vector overlaid on frame 16 indicate the total drift during the whole manipulation process from the first frame (not shown) to the frame number 16. The Si atom in frame 14 was laying near a defect as highlighted, while the lattice structure in the same area after the replacement with C atom looks pristine as highlighted in frame 16.

3.4.3 Replacement of Si by C

One of the limitations of single-atom manipulation is having the impurity we want to manipulate disappear under the electron beam. Figure 3.9 shows a single Si atom during automated manipulation, which was not manipulatable despite having a 3-fold configuration. After 15 unsuccessful frames, the Si, probably due to the nearby defect, was lost from the lattice and replaced by a C atom. The drift during the process was considerable, with a total drift of 0.7 nm for the 16 recorded frames, which corresponds to about 0.4 Å per frame. Since the target site is defined by its pixel coordinates in the image and not a physical atomic site, we can see how drift between frames 14 and 15 caused a change in the defined lattice site.

3.4.4 Ejection of C neighbor to Al

Automated manipulation of a single-atom impurity is achieved by parking the electron beam on a C neighbor to induce a bond inversion between them, having the impurity move through the lattice as explained before. Nevertheless, sometimes this leads to knock-on damage of the C atom under the electron beam and as a result the dopant transforms from 3-fold to 4-fold configuration. Figure 3.11 shows a 3-fold Al atom during automated manipulation turned into 4-fold as a result of this AlCKO process. After that two additional C atoms were lost forming a defect at which the Al atom was moved. The EEL spectrum of the Al atom is depicted in Figure 3.10, which shows the Al $L_{2,3}$ core-loss edge at 73 eV.

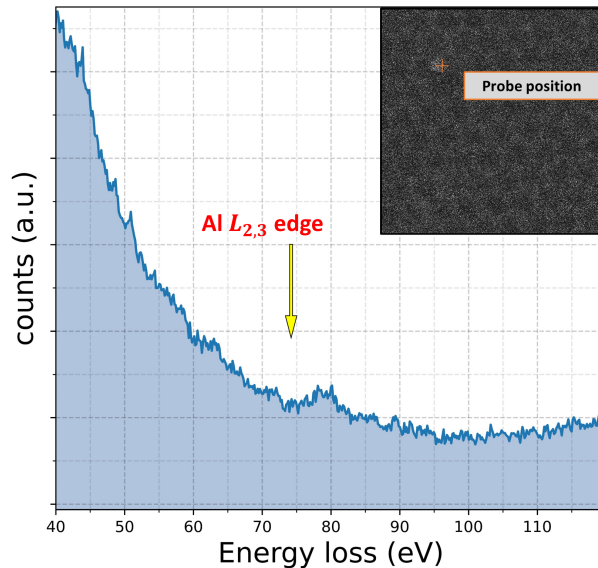


Figure 3.10: EEL spectrum of the single-atom dopant (shown in the MAADF image in the inset of the figure) with a small feature starting at about 73 eV, which corresponds to the Al $L_{2,3}$ energy-loss edge.

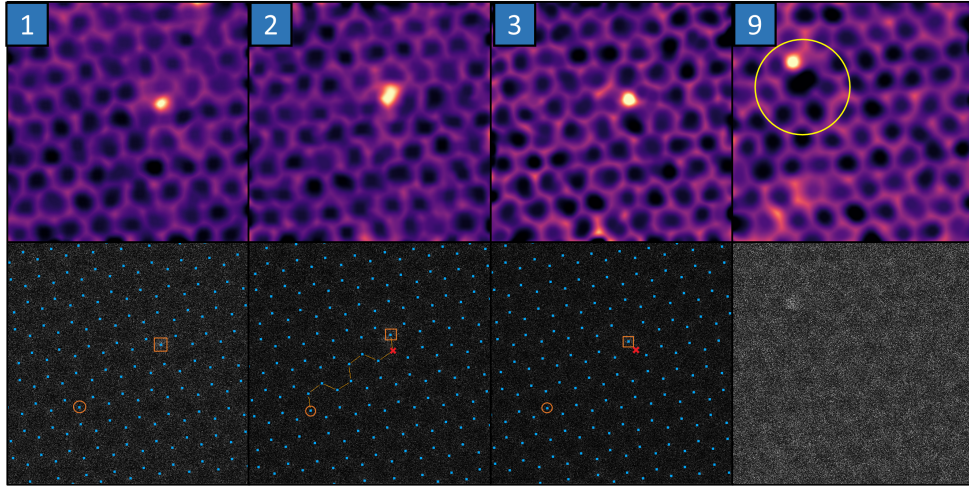


Figure 3.11: MAADF image series during a manipulation trial of single Al atom. During the process, the 3-fold Al dopant transformed into 4-fold (between frame 2 and 3) due to the knock-on damage of one of its C neighbors. The continuation of the manipulation trial led then to knock-on damage of two additional C atoms and creating a defect with the Al impurity. After that the structure recognition failed and the manipulation process was terminated as shown in frame 9.

3.4.5 Successful automated manipulation of Al dopant

It was not until six months of work in this project that we were able to successfully manipulate a single-atom Al impurity. The manipulation process is depicted in Figure 3.12, in which the Al atom first performed a single jump (between frames 4 and 5), then sample drift caused a change in the relative position between the target site and the Al atom (between frames 5, 10 and 11). After that it committed an uncontrolled jump to a different lattice site than the one defined by the calculated path (between frames 17 and 18). Then it performed two successive controlled jumps to reach its defined target site (between frames 18 and 22). The EEL spectrum of the single atom depicted in Figure 3.13 shows that the single dopant was an Al atom.

3.4.6 Ejection of Al

During our manipulation experiments of Si, it was noticed that whenever the Si atom was lost from the lattice, it had been replaced by carbon. This was not the case for the Al impurities, which leave behind vacant lattice sites presumably after being ejected by the electron beam from the graphene lattice. This was first noticed when acquiring EEL spectrum of an Al atom, where it was removed from the lattice during the irradiation as shown in Figure 3.14.b. Notably, this is reminiscent of the first EELS confirmation of an incidental Al dopant reported by Su [9]. The spectrum recorded (shown in Figure 3.14.a

3.4 Automated single-atom manipulation

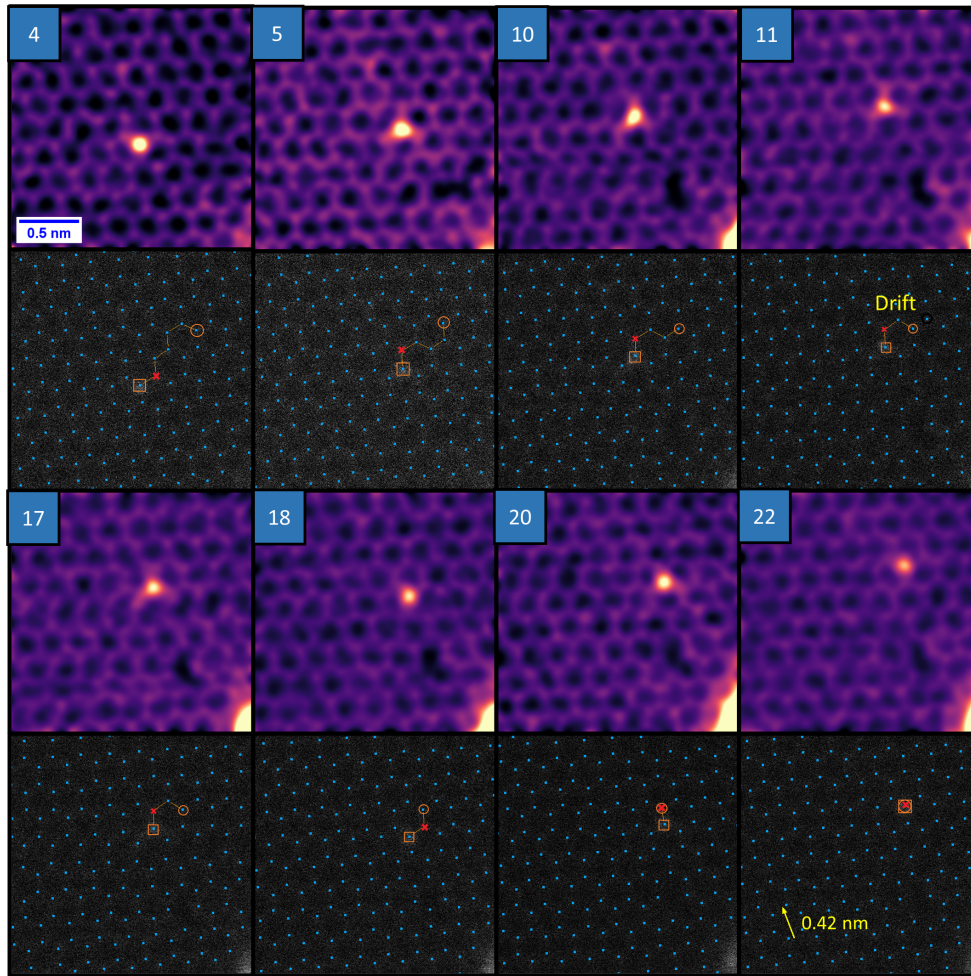


Figure 3.12: MAADF image sequence showing automated manipulation of an Al atom. The Al exchanged its position successfully with the target C atom (between frames 4 and 5), then it moved to an undesired lattice site. After that it made two successful jumps (between frames 18 and 22) to eventually reach its defined target site .

was one of the best Al single-atom spectrum I could obtain during the whole project, but the atom was gone and no manipulation trial could be performed. Thus later when I was finding single atoms that I suspected are Al from their contrast, I was in most cases starting with the manipulation experiment before recording their EEL spectrum. Figure 3.15 shows an AlKO event during automated single-atom manipulation, in which after the 3-fold dopant was removed from the lattice in frame 5 leaving behind a SV. The created vacancy was not immediately healed by a migrating carbon atom afterwards, which allowed us to image the area with a larger FOV afterwards as shown in Figure 3.15.b.

3 Results and discussion

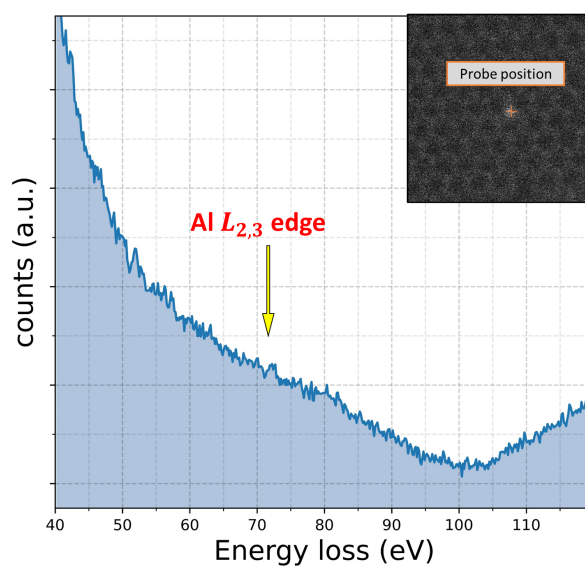


Figure 3.13: EEL spectrum of the Al atom (shown in the inset MAADF image) that successfully performed three controlled jumps under the electron beam, with an energy-loss edge at around 73 eV. The signal is very weak, but apart from the spectrometer reflection, there is no indication of the Si edge.

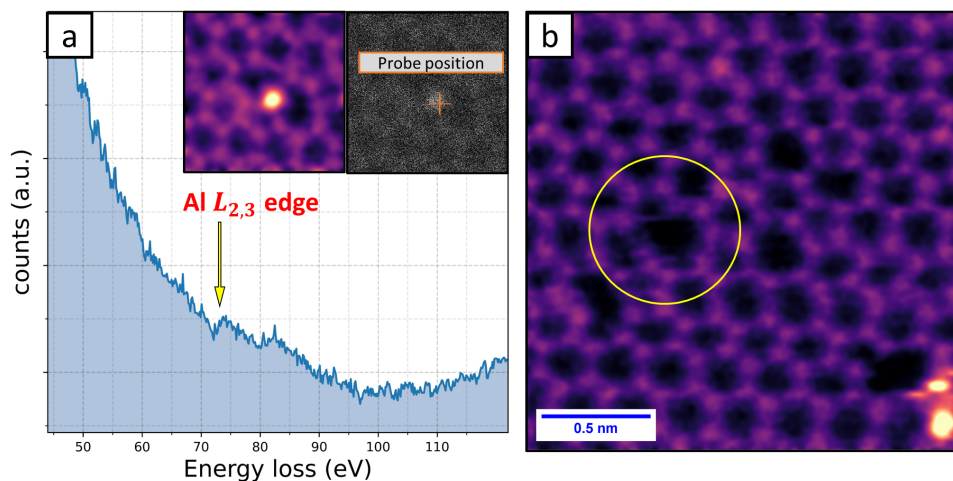


Figure 3.14: A single Al impurity was knocked out during recording its spectrum. (a) EEL spectrum of an Al atom showing the core-loss edge at 73 eV (with the atom depicted in the inset colored MAADF image). (b) An image of the vacant site left after the Al atom was removed from the lattice during spectrum acquisition.

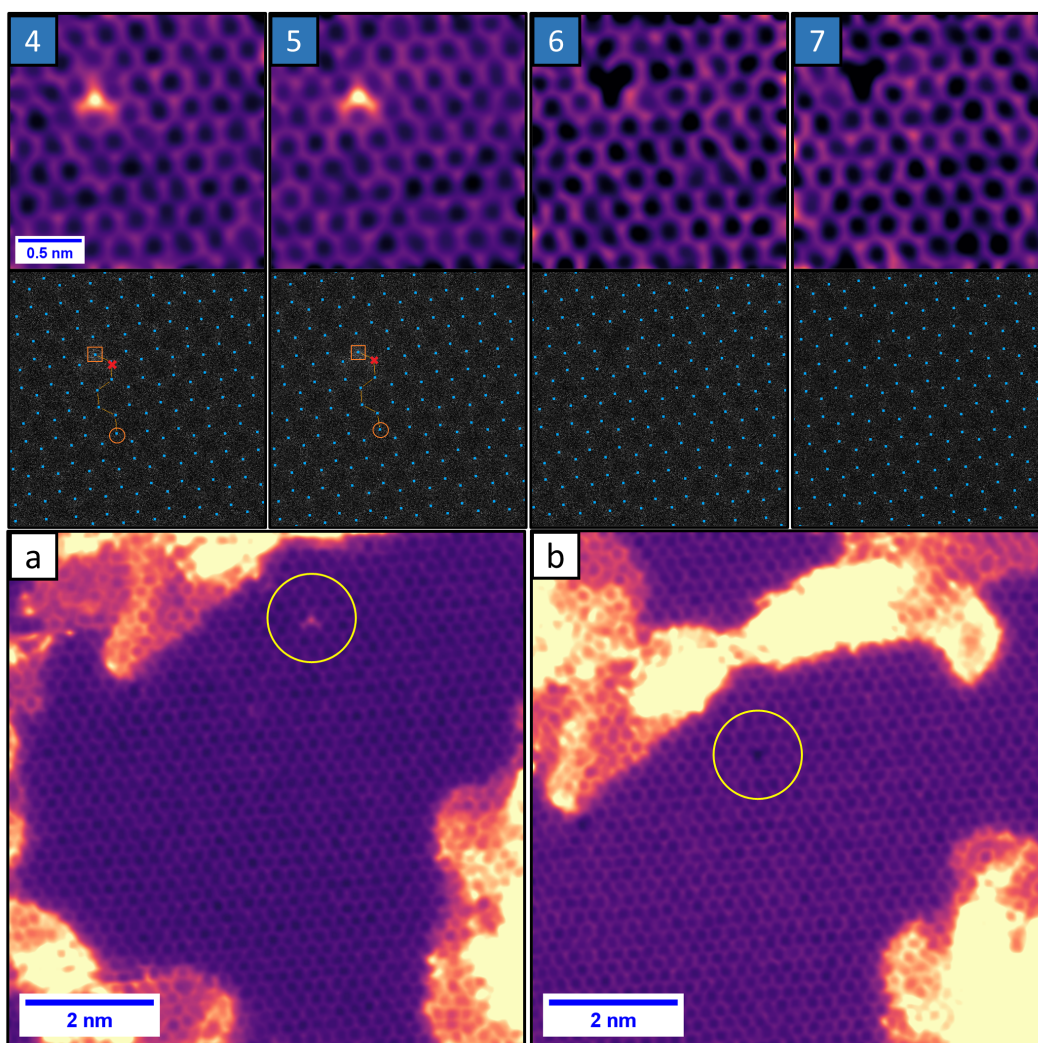


Figure 3.15: MAADF image series of automated Al manipulation showing an AIKO event, in which the Al dopant was ejected from the lattice. (a) and (b) are two images of the area where the Al atom (marked by yellow circle) was knocked out before and after the attempted manipulation (FOV = 8 nm).

3.5 Challenges and limitations

Since the beginning of this master project, it was emphasized to me that having a sample with the desired impurity species and in conditions suitable for automated single-atom manipulation is one of the major challenges to be overcome. It was not until November 2022, five months after the beginning of this work, that we succeeded in depositing Al impurities on the graphene samples.

Another major obstacle that limits the success of single-atom automated manipulation is related to the software and how it is integrated with the instrument. As an example, during one of the experiments, after the Si atom reached its defined target site, the plugin switched to the next recognized impurity to manipulate it to its user-defined target site as well. But after a few frames due to the drift, the target site of the first successfully manipulated Si atom was shifted with respect to it and the manipulator switched back to attempt to manipulate it again. Thus compensation of the sample drift should be integrated into the software, or a sample stage with an even higher degree of mechanical stability would be essential for successful automated single-atom manipulation.

The last major limitation I will be listing here is perhaps the most important one: the physical limitation represented by the undesired competing processes that can occur during automated manipulation and terminate the process, such as the carbon replacement process or the knock-on damage of a C neighbor that leaves behind a 4-fold impurity that is not manipulatable.

Since the replacement process involves a C adatom, it could potentially be suppressed by lowering the sample temperature. Knock-on damage can never be completely avoided, but drift compensation could allow a lower primary beam energy to be practically used, which has been shown for Si to increase the number of successful jumps.

4 Conclusion

In this thesis, the automated manipulation of both Si and Al single-atom impurities within the graphene lattice was demonstrated. This was achieved via direct positional exchange between the impurity and one of its carbon neighbor utilizing the focused electron probe of a scanning transmission electron microscope. While the hope of forming patterns out of the manipulated atoms could not be reached, 67 successful automated manipulations of Si single-atoms were recorded by the end of this project. Regarding the manipulation of Al impurities, only 12 successful manipulation events could be recorded, which were characterized via recording their EEL spectra and their Z -contrast.

Graphene sample with single Al impurities was prepared during this work via a two-step process. This was achieved by first forming single vacancy defects in the graphene lattice using Ar^+ plasma irradiation that serve as recipients for 3-fold single-atom dopants, followed by thermal evaporation for depositing Al onto the sample. Vacuum annealing using a diode laser was used for both defect healing and for cleaning the sample from contamination, while the STEM column laser was occasionally used for getting rid of mobile contamination.

Although the dream of patterning using automated single-atom manipulation was eventually not achieved, being active in this project and being able to practice engineering on the atomic level gave great pleasure and excitement. I believe that overcoming the limitations and difficulties mentioned before we would be able to achieve this goal one day. Having a solution to compensate for the drift, being able to fabricate samples with the desired defect density and types in addition to improving software-related issues, and perhaps using an instrument dedicated for the purpose of single-atom manipulation with a high mechanical stability of the sample stage and cryogenic cooling, could together make automated single-atom manipulation a practical tool for research and beyond.

Bibliography

- [1] Kostya S Novoselov, Andre K Geim, Sergei V Morozov, De-eng Jiang, Yanshui Zhang, Sergey V Dubonos, Irina V Grigorieva, and Alexandr A Firsov. Electric field effect in atomically thin carbon films. *Science*, 306(5696):666–669, 2004.
- [2] Andre K Geim and Konstantin S Novoselov. The rise of graphene. In *Nanoscience and technology: a collection of reviews from nature journals*, pages 11–19. World Scientific, 2010.
- [3] A. H. Castro Neto, F. Guinea, N. M. R. Peres, K. S. Novoselov, and A. K. Geim. The electronic properties of graphene. *Rev. Mod. Phys.*, 81(1):109, 2009.
- [4] Andre Konstantin Geim. Graphene: status and prospects. *Science*, 324(5934):1530–1534, 2009.
- [5] Mukesh Tripathi, Alexander Markevich, Roman Böttger, Stefan Facsko, Elena Besley, Jani Kotakoski, and Toma Susi. Implanting germanium into graphene. *ACS Nano*, 12(5):4641–4647, 2018.
- [6] Ousoo Kim. Seeing the world of nanotechnology from a single-molecule perspective. *RIKEN Research*, 6(6), June 2011.
- [7] Mukesh Tripathi, Andreas Mittelberger, Nicholas A Pike, Clemens Mangler, Jannik C Meyer, Matthieu J Verstraete, Jani Kotakoski, and Toma Susi. Electron-beam manipulation of silicon dopants in graphene. *Nano Letters*, 18(8):5319–5323, 2018.
- [8] Toma Susi, Jani Kotakoski, Demie Kepaptsoglou, Clemens Mangler, Tracy C Lovejoy, Ondrej L Krivanek, Recep Zan, Ursel Bangert, Paola Ayala, Jannik C Meyer, et al. Silicon–carbon bond inversions driven by 60-keV electrons in graphene. *Physical Review Letters*, 113(11):115501, 2014.
- [9] Cong Su, Mukesh Tripathi, Qing-Bo Yan, Zegao Wang, Zihan Zhang, Christoph Hofer, Haozhe Wang, Leonardo Basile, Gang Su, Mingdong Dong, et al. Engineering single-atom dynamics with electron irradiation. *Science Advances*, 5(5):eaav2252, 2019.
- [10] Georg Zagler, Maximilian Stecher, Alberto Trentino, Fabian Kraft, Cong Su, Andreas Postl, Manuel Längle, Christian Pesenhofer, Clemens Mangler, E Harriet Åhlgren, et al. Beam-driven dynamics of aluminium dopants in graphene. *2D Materials*, 9(3):035009, 2022.

- [11] Catherine E Housecroft and Edwin C Constable. *Chemistry: an introduction to organic, inorganic and physical chemistry*. Pearson education, 2010.
- [12] Luis EF Foa Torres, Stephan Roche, and Jean-Christophe Charlier. *Introduction to graphene-based nanomaterials: from electronic structure to quantum transport*. Cambridge University Press, 2014.
- [13] Phaedon Avouris, Tony F Heinz, and Tony Low. *2D Materials*. Cambridge University Press, 2017.
- [14] Mikhail I. Katsnelson. *The Physics of Graphene*. Cambridge University Press, 2nd edition, 2020.
- [15] Lili Liu, Miaoqing Qing, Yibo Wang, and Shimou Chen. Defects in graphene: generation, healing, and their effects on the properties of graphene: a review. *Journal of Materials Science & Technology*, 31(6):599–606, 2015.
- [16] Florian Banhart, Jani Kotakoski, and Arkady V Krasheninnikov. Structural defects in graphene. *ACS Nano*, 5(1):26–41, 2011.
- [17] Derek Hull and David J Bacon. *Introduction to dislocations*, volume 37. Elsevier, 2011.
- [18] Juan Jose Palacios, Joaquin Fernández-Rossier, and Luis Brey. Vacancy-induced magnetism in graphene and graphene ribbons. *Physical Review B*, 77(19):195428, 2008.
- [19] Jianmei Yuan, Zhe Wei, Jianxin Zhong, Yanping Huang, and Yuliang Mao. Point defects engineering in graphene/h-bn bilayer: A first principle study. *Applied Surface Science*, 320:502–508, 2014.
- [20] Thomas Trevethan, Christopher D Latham, Malcolm I Heggie, Patrick R Briddon, and Mark J Rayson. Vacancy diffusion and coalescence in graphene directed by defect strain fields. *Nanoscale*, 6(5):2978–2986, 2014.
- [21] AA El-Barbary, RH Telling, CP Ewels, MI Heggie, and PR Briddon. Structure and energetics of the vacancy in graphite. *Physical Review B*, 68(14):144107, 2003.
- [22] Soumyajyoti Haldar, Rodrigo G Amorim, Biplab Sanyal, Ralph H Scheicher, and Alexandre R Rocha. Energetic stability, stm fingerprints and electronic transport properties of defects in graphene and silicene. *RSC Advances*, 6(8):6702–6708, 2016.
- [23] Andreas Postl. *Towards automated atom manipulation in the scanning transmission electron microscope*. PhD thesis, Faculty of Physics, University of Vienna, 2022.
- [24] Ottorino Ori, Franco Cataldo, and Mihai V Putz. Topological anisotropy of stone-wales waves in graphenic fragments. *International Journal of Molecular Sciences*, 12(11):7934–7949, 2011.

Bibliography

- [25] Elif Ertekin, DC Chrzan, and Murray S Daw. Topological description of the stone-wales defect formation energy in carbon nanotubes and graphene. *Physical Review B*, 79(15):155421, 2009.
- [26] Chintamani Nagesa Ramachandra Rao, Kailash Gopalakrishnan, and A Govindaraj. Synthesis, properties and applications of graphene doped with boron, nitrogen and other elements. *Nano Today*, 9(3):324–343, 2014.
- [27] Guo Hong, Qi-Hui Wu, Chundong Wang, Jianguo Ren, Tingting Xu, Wenjun Zhang, and Shuit-Tong Lee. Surface doping of nitrogen atoms on graphene via molecular precursor. *Applied Physics Letters*, 102(5):051610, 2013.
- [28] Hongtao Wang, Qingxiao Wang, Yingchun Cheng, Kun Li, Yingbang Yao, Qiang Zhang, Cezhou Dong, Peng Wang, Udo Schwingenschlögl, Wei Yang, et al. Doping monolayer graphene with single atom substitutions. *Nano Letters*, 12(1):141–144, 2012.
- [29] Philip Willke, Julian A Amani, Anna Sinterhauf, Sangeeta Thakur, Thomas Kotzott, Thomas Druga, Steffen Weikert, Kalobaran Maiti, Hans Hofsäss, and Martin Wenderoth. Doping of graphene by low-energy ion beam implantation: structural, electronic, and transport properties. *Nano Letters*, 15(8):5110–5115, 2015.
- [30] Demie Kepaptsoglou, Trevor P Hardcastle, Che R Seabourne, Ursel Bangert, Recep Zan, Julian Alexander Amani, Hans Hofsäss, Rebecca J Nicholls, Rik MD Brydson, Andrew J Scott, et al. Electronic structure modification of ion implanted graphene: the spectroscopic signatures of p-and n-type doping. *ACS Nano*, 9(11):11398–11407, 2015.
- [31] U Bangert, William Pierce, DM Kepaptsoglou, Q Ramasse, R Zan, MH Gass, JA Van den Berg, CB Boothroyd, J Amani, and H Hofsäss. Ion implantation of graphene toward ic compatible technologies. *Nano Letters*, 13(10):4902–4907, 2013.
- [32] Alberto Trentino, Kenichiro Mizohata, Georg Zagler, Manuel Längle, Kimmo Mustonen, Toma Susi, Jani Kotakoski, and E Harriet Åhlgren. Two-step implantation of gold into graphene. *2D Materials*, 9(2):025011, 2022.
- [33] Alex W Robertson, Barbara Montanari, Kuang He, Judy Kim, Christopher S Allen, Yimin A Wu, Jaco Olivier, Jan Neethling, Nicholas Harrison, Angus I Kirkland, et al. Dynamics of single fe atoms in graphene vacancies. *Nano Letters*, 13(4):1468–1475, 2013.
- [34] Pin-Cheng Lin, Renan Villarreal, Simona Achilli, Harsh Bana, Maya N Nair, Antonio Tejada, Ken Verguts, Stefan De Gendt, Manuel Auge, Hans Hofsäss, et al. Doping graphene with substitutional mn. *ACS Nano*, 15(3):5449–5458, 2021.
- [35] Hao Wang, Jiting Tian, Linxin Guo, Xun Guo, Zhanfeng Yan, Jian Zheng, Qijie Feng, Wei Zhou, and Jianming Xue. Computational study of low-energy Pt-Ion

- implantation into graphene for single-atom catalysis. *ACS Applied Nano Materials*, 2022.
- [36] Toma Susi, Trevor P Hardcastle, Hans Hofsäss, Andreas Mittelberger, Timothy J Pennycook, Clemens Mangler, Rik Drummond-Brydson, Andrew J Scott, Jannik C Meyer, and Jani Kotakoski. Single-atom spectroscopy of phosphorus dopants implanted into graphene. *2D Materials*, 4(2):021013, 2017.
- [37] Wu Zhou, Myron D Kapetanakis, Micah P Prange, Sokrates T Pantelides, Stephen J Pennycook, and Juan-Carlos Idrobo. Direct determination of the chemical bonding of individual impurities in graphene. *Physical Review Letters*, 109(20):206803, 2012.
- [38] Petri O Lehtinen, Adam S Foster, A Ayuela, Arkady Krasheninnikov, Kai Nordlund, and Risto M Nieminen. Magnetic properties and diffusion of adatoms on a graphene sheet. *Physical Review Letters*, 91(1):017202, 2003.
- [39] David A Porter and Kenneth E Easterling. *Phase transformations in metals and alloys*. CRC press, 2009.
- [40] Helmut Mehrer and Nicolaas A Stolwijk. *Heroes and highlights in the history of diffusion*. 2009.
- [41] Sami Malola, Hannu Häkkinen, and Pekka Koskinen. Gold in graphene: In-plane adsorption and diffusion. *Applied Physics Letters*, 94(4):043106, 2009.
- [42] Kenjiro Oura, VG Lifshits, AA Saranin, AV Zotov, and M Katayama. *Surface science: an introduction*. Springer Science & Business Media, 2013.
- [43] Florian Banhart. Irradiation effects in carbon nanostructures. *Reports on Progress in Physics*, 62(8):1181, 1999.
- [44] Toma Susi, Jani Kotakoski, Raul Arenal, Simon Kurasch, Hua Jiang, Viera Skakalova, Odile Stephan, Arkady V Krasheninnikov, Esko I Kauppinen, Ute Kaiser, et al. Atomistic description of electron beam damage in nitrogen-doped graphene and single-walled carbon nanotubes. *ACS Nano*, 6(10):8837–8846, 2012.
- [45] Toma Susi, Jannik C Meyer, and Jani Kotakoski. Quantifying transmission electron microscopy irradiation effects using two-dimensional materials. *Nature Reviews Physics*, 1(6):397–405, 2019.
- [46] Ludwig Reimer. *Transmission electron microscopy: physics of image formation and microanalysis*, volume 36. Springer, 2013.
- [47] OS Oen. Cross sections for atomic displacements in solids by fast electrons. Technical report, Oak Ridge National Lab., Tenn.(USA), 1973.

Bibliography

- [48] Jannik C Meyer, Franz Eder, Simon Kurasch, Viera Skakalova, Jani Kotakoski, Hye Jin Park, Siegmur Roth, Andrey Chuvilin, Sören Eyhusen, Gerd Benner, et al. Accurate measurement of electron beam induced displacement cross sections for single-layer graphene. *Physical Review Letters*, 108(19):196102, 2012.
- [49] Alexandru Ionut Chirita Mihaila, Toma Susi, and Jani Kotakoski. Influence of temperature on the displacement threshold energy in graphene. *Scientific Reports*, 9(1):12981, 2019.
- [50] D.B. Williams and C.B. Carter. *Transmission Electron Microscopy: A Textbook for Materials Science*. Number Bd. 2 in Cambridge library collection. Springer US, 2009.
- [51] Mukesh Tripathi. *Modifying low-dimensional materials using energetic charged particles*. PhD thesis, 2019.
- [52] NJ Bacon, GJ Corbin, N Dellby, P Hrcirik, OL Krivanek, A McManama-Smith, MF Murfitt, and ZS Szilagy. Nion ultrastem: an aberration-corrected stem for imaging and analysis. *Microscopy and Microanalysis*, 11(S02):1422–1423, 2005.
- [53] Ray F Egerton. *Electron energy-loss spectroscopy in the electron microscope*. Springer Science & Business Media, 2011.
- [54] Ferdinand Hofer, Franz-Philipp Schmidt, Werner Grogger, and Gerald Kothleitner. Fundamentals of electron energy-loss spectroscopy. In *IOP conference Series: Materials Science and Engineering*, volume 109, 2016.
- [55] Sònia Estradé Albiol. Electron energy loss spectroscopy: physical principles, state of the art and applications to the nanosciences. *Capítol del llibre: Handbook of instrumental techniques for materials, chemical and biosciences research, Centres Científics i Tecnològics. Universitat de Barcelona, Barcelona, 2012. Part I. Materials technologies (MT), MT. 2, 12 p., 2012.*
- [56] Quentin M Ramasse, Che R Seabourne, Despoina-Maria Kepaptsoglou, Recep Zan, Ursel Bangert, and Andrew J Scott. Probing the bonding and electronic structure of single atom dopants in graphene with electron energy loss spectroscopy. *Nano Letters*, 13(10):4989–4995, 2013.
- [57] AV Krasheninnikov and FJNM Banhart. Engineering of nanostructured carbon materials with electron or ion beams. *Nature Materials*, 6(10):723–733, 2007.
- [58] Marika Schleberger and Jani Kotakoski. 2D material science: Defect engineering by particle irradiation. *Materials*, 11(10):1885, 2018.
- [59] E Balanzat and S Bouffard. Basic phenomena of the particle-matter interaction. In *Solid State Phenomena*, volume 30, pages 7–74. Trans Tech Publ, 1992.
- [60] Bozhong Zhuang, Shiyun Li, Siyang Li, and Jun Yin. Ways to eliminate pmma residues on graphene—super-clean graphene. *Carbon*, 173:609–636, 2021.

- [61] Clemens Mangler, Jannik Meyer, Andreas Mittelberger, Kimmo Mustonen, Toma Susi, and Jani Kotakoski. A materials scientist's CANVAS: A system for controlled alteration of nanomaterials in vacuum down to the atomic scale. *Microscopy and Microanalysis*, 28(S1):2940–2942, 2022.
- [62] SPECS Surface Nano Analysis GmbH. *Application Note: Atom Source Mode*. Voltastrasse 5, 13355 Berlin, Germany.
- [63] AN Agnihotri, AH Kelkar, S Kasthurirangan, KV Thulasiram, CA Desai, WA Fernandez, and LC Tribedi. An ecr ion source-based low-energy ion accelerator: development and performance. *Physica Scripta*, 2011(T144):014038, 2011.
- [64] Alberto Trentino, Jacob Madsen, Andreas Mittelberger, Clemens Mangler, Toma Susi, Kimmo Mustonen, and Jani Kotakoski. Atomic-level structural engineering of graphene on a mesoscopic scale. *Nano Letters*, 21(12):5179–5185, 2021.
- [65] Márcia Maria Lucchese, F Stavale, EH Martins Ferreira, Cecilia Vilani, Marcus Vinicius de Oliveira Moutinho, Rodrigo B Capaz, Carlos Alberto Achete, and A Jorio. Quantifying ion-induced defects and raman relaxation length in graphene. *Carbon*, 48(5):1592–1597, 2010.
- [66] SPECS Surface Nano Analysis GmbH. *MPS-ECR Plasma Cracker Source*, 2013.
- [67] Donald M Mattox. *Handbook of physical vapor deposition (PVD) processing*. William Andrew, 2010.
- [68] Christopher Muratore, Andrey A Voevodin, and Nicholas R Glavin. Physical vapor deposition of 2D Van der Waals materials: a review. *Thin Solid Films*, 688:137500, 2019.
- [69] Donald M Mattox and VH Mattox. *Vacuum coating technology*. Springer, 2003.
- [70] David R Lide. *CRC handbook of chemistry and physics*, volume 85. CRC press, 2004.
- [71] Toma Susi, Jannik C Meyer, and Jani Kotakoski. Manipulating low-dimensional materials down to the level of single atoms with electron irradiation. *Ultramicroscopy*, 180:163–172, 2017.
- [72] Mukesh Tripathi, Andreas Mittelberger, Nicholas A Pike, Clemens Mangler, Jannik C Meyer, Matthieu J Verstraete, Jani Kotakoski, and Toma Susi. Electron-beam manipulation of silicon dopants in graphene. *Nano Letters*, 18(8):5319–5323, 2018.
- [73] Andreas Postl, Jacob Madsen, Christoph Hofer, Clemens Mangler, Andreas Mittelberger, and Toma Susi. Python Package "Nion Swift Atom Manipulator". doi:11353/10.1586606, 2021.
- [74] Harold W Kuhn. The hungarian method for the assignment problem. *Naval research logistics quarterly*, 2(1-2):83–97, 1955.

Bibliography

- [75] Roy Jonker and Ton Volgenant. Improving the hungarian assignment algorithm. *Operations Research Letters*, 5(4):171–175, 1986.
- [76] Lewys Jones, Richard Beanland, Sergio Lozano-Perez, Karim Baba-kishi, and Peter D Nellist. Improving the SNR of Atomic Resolution STEM EELS & EDX Mapping while Reducing Beam-damage by using Non-rigid Spectrum-image Averaging. *Microscopy and Microanalysis*, 21(S3):1215–1216, 2015.
- [77] Ossi Lehtinen, Jani Kotakoski, AV Krasheninnikov, Antti Tolvanen, Kai Nordlund, and Juhani Keinonen. Effects of ion bombardment on a two-dimensional target: Atomistic simulations of graphene irradiation. *Physical Review B*, 81(15):153401, 2010.
- [78] SPECS GmbH - Surface Analysis and Computer Technology. Mini ECR Plasma Source MPS-ECR. Company information sheet, 2006. <http://www.specs.de>.
- [79] Tieshan Yang, Han Lin, Xiaorui Zheng, Kian Ping Loh, and Baohua Jia. Tailoring pores in graphene-based materials: from generation to applications. *Journal of Materials Chemistry A*, 5(32):16537–16558, 2017.
- [80] Aspasia Antonelou, Labrini Sygellou, Katerina Vrettos, Vasilios Georgakilas, and Spyros N Yannopoulos. Efficient defect healing and ultralow sheet resistance of laser-assisted reduced graphene oxide at ambient conditions. *Carbon*, 139:492–499, 2018.
- [81] Lili Liu, Miaoqing Qing, Yibo Wang, and Shimou Chen. Defects in graphene: generation, healing, and their effects on the properties of graphene: a review. *Journal of Materials Science & Technology*, 31(6):599–606, 2015.
- [82] Carsten Speckmann, Julia Lang, Jacob Madsen, Mohammad Reza Ahmadpour Monazam, Georg Zagler, Gregor T Leuthner, Niall McEvoy, Clemens Mangler, Toma Susi, and Jani Kotakoski. Combined electronic excitation and knock-on damage in monolayer MoS₂. *Physical Review B*, 107(9):094112, 2023.
- [83] Jani Kotakoski, Clemens Mangler, and Jannik C Meyer. Imaging atomic-level random walk of a point defect in graphene. *Nature Communications*, 5(1):1–5, 2014.